1 *In vivo* chromatic and spatial tuning of foveolar retinal ganglion cells in *Macaca fascicularis*

2

3 Tyler Godat*[1,2], Nicolas P. Cottaris[3], Sara Patterson[1], Kendall Kohout[1,2], Keith Parkins[1], Qiang

4 Yang[1], Jennifer M. Strazzeri[1,4], Juliette E. McGregor[1], David H. Brainard[3], William H. Merigan[1,4] &

5 David R. Williams*[1,2,4]

6 [1] Center for Visual Science, University of Rochester, Rochester, NY, United States of America.

7 [2] Institute of Optics, University of Rochester, Rochester, NY, United States of America.

8 [3] Department of Psychology, University of Pennsylvania, Philadelphia, PA, United States of

9 America.

10 [4] David & Ilene Flaum Eye Institute, University of Rochester Medical Center, Rochester, NY,

11 United States of America.

12 * Corresponding authors

13 E-mail: tgodat@ur.rochester.edu (TG), david.williams@rochester.edu (DRW)

14

15

Abstract

The primate fovea is specialized for high acuity chromatic vision, with the highest density of cone photoreceptors and a disproportionately large representation in visual cortex. The unique visual properties conferred by the fovea are conveyed to the brain by retinal ganglion cells, the somas of which lie at the margin of the foveal pit. Microelectrode recordings of these centermost retinal ganglion cells have been challenging due to the fragility of the fovea in the excised retina. Here we overcome this challenge by combining high resolution fluorescence adaptive optics ophthalmoscopy with calcium imaging to optically record functional responses of foveal retinal ganglion cells in the living eye. We use this approach to study the chromatic responses and spatial transfer functions of retinal ganglion cells using spatially uniform fields modulated in different directions in color space and monochromatic drifting gratings. We recorded from over 350 cells across three *Macaca fascicularis* primates over a time period of weeks to months. We find that the majority of the L vs. M cone opponent cells serving the most central foveolar cones have spatial transfer functions that peak at high spatial frequencies (20-40 c/deg), reflecting strong surround inhibition that sacrifices sensitivity at low spatial frequencies but preserves the transmission of fine detail in the retinal image. In addition, we fit to the drifting grating data a detailed model of how ganglion cell responses draw on the cone mosaic to derive receptive field properties of L vs. M cone opponent cells at the very center of the foveola. The fits are consistent with the hypothesis that foveal midget ganglion cells are specialized to preserve information at the resolution of the cone mosaic. By characterizing the functional properties of retinal ganglion cells *in vivo* through adaptive optics, we characterize the response characteristics of these cells *in situ*.

Introduction

In primates, the fovea is a specialized region of the retina characterized by a high density of cones at its center and a corresponding radial displacement of retinal cells and retinal vasculature. These specializations, along with a correspondingly expanded representation of the central visual field in cortex [1-3], contribute to the superiority of foveal vision relative to peripheral vision in spatial resolution and color discrimination [1, 4-21]. To date, in excess of 20 classes of retinal ganglion cells (RGCs) have been identified in macaque retina [1, 4, 6, 7, 13, 17-20, 22-52], reflecting a complex array of retinal computations that precede additional processing in the brain. Despite these advances, a complete understanding of these independent circuits and their role in vision and behavior remains elusive. Even the precise role and scope of function of the most numerous and commonly studied RGCs, the midget ganglion cells, remains controversial, and there has been relatively little study at the very center of the foveola.

Electrophysiological responses from primate RGCs have been studied *in vivo* with a microelectrode that penetrates the sclera [53, 54] and *in vitro* using a single microelectrode [6, 27] or microelectrode arrays [55, 56]. However, the majority of the recordings in primate have been made in peripheral retina, often 30 to 70 degrees from the fovea due to the fragility of the fovea.The survival of an excised fovea is time limited, and the delicate structure of the foveal pit is often strained when flattened, sometimes tearing crucial circuitry. While the anatomical basis for foveal circuitry has been studied extensively [7, 32, 34, 38, 57, 58] and there has been some *ex vivo* physiology of foveal RGCs, most individual cell classes present in the primate fovea have not been directly studied, especially at the most central locations. Retinal processing can also be inferred by recording from retinorecipient neurons in the LGN, but the foveal representation of

62 the LGN is located within a relatively thin cell layer making such recordings challenging [59].
63 Moreover, it has been difficult to identify the exact foveal center *in vivo* and determining the
64 precise retinal eccentricity of single cell recordings in LGN is difficult [5, 9, 60-62]. Furthermore,
65 RGCs project to many different targets other than LGN, so studying these cells at the retinal level
66 gives the best chance at providing a more complete sampling.
67
68 In this study, we use functional adaptive optics cellular imaging in the living eye (FACILE) [12, 16,
69 63, 64], a technique that utilizes an adaptive optics scanning light ophthalmoscope (AOSLO) to
70 image fluorescence elicited from the activity of RGCs that express genetically encoded calcium
71 indicators, such as those described by Chen et al [65]. Simultaneously, the cone mosaic is imaged
72 with infrared wavelengths to map the cone density profile at the fovea. The cone mosaic images
73 have a relatively high signal to noise ratio (SNR) and are also used to track residual eye motion in
74 the fluorescence channel which has a relatively low SNR. Knowing the cone density profile for an
75 individual subject allows for a more precise modeling of receptive field structure and more precise
76 motion correction. Using this technique, we can both image and stimulate the centermost
77 foveolar cones with spatial or chromatic stimuli and optically record the activity of the ganglion
78 cells that are served by those cones, characterizing the physiology of the innermost foveal primate
79 RGCs *in vivo*. Indeed, we can return repeatedly to the same ganglion cells for weeks to months,
80 allowing repeated functional measures of the same cells. With this approach, we can use data
81 from an individual animal that includes the optics, the cone density profile, and the RGC responses
82 to create a detailed model of the first stages of visual processing.
83

84 # Materials and methods

Animal care

The macaques (*Macaca fascicularis)* were housed in pairs in an AAALAC accredited facility. They had free access to food and water, providing a complete and nutritious diet. To supplement their ordinary lab chow, animals were given various treats daily such as nuts, raisins, and a large variety of fresh fruits and vegetables. An animal behaviorist provided novel enrichment items once per week, including items such as grass and treat filled bags, grapevines, and forage boxes. Daily enrichment included several pieces of manipulata: mirrors, puzzle feeders rotated among the animals, daily movies and/or music, as well as rotating access to a large free-ranging space with swings and elevated perches during any long periods between imaging sessions. All macaques were cared for by the Department of Comparative Medicine veterinary staff, including four full-time veterinarians, five veterinary technicians, and an animal care staff who monitored animal health and checked for signs of discomfort at least twice daily. This study was carried out in strict accordance with the Association for Research in Vision and Ophthalmoscopy (ARVO) Statement for the Use of Animals and the recommendations in the Guide for the Care and Use of Laboratory Animals of the National Institutes of Health. The protocol was approved by the University Committee on Animal Resources of the University of Rochester (PHS assurance number: D16-00188(A3292-01)).

Immune suppression

Two macaques (M2, M3) received subcutaneous Cyclosporine A prior to intravitreal injection and imaging. Blood trough levels were collected weekly to titrate the dose into a therapeutic range of 150-200 ng ml^{-1} and then maintained at that level. M2 began immune suppression in March 2018 with 6 mg kg^{-1}, then stepped down a month later to 4 mg kg^{-1} which was maintained until October

108 2019 when suppression was stopped following the completion of all experiments used in this
109 manuscript. M3 started immune suppression in May 2019 at 6 mg kg^{-1}, then stepped down to 3.4
110 mg kg^{-1} which continues at time of submission. M1 did not receive any immune suppression.
111 Current best practice for primate imaging in our lab has all new animals receiving immune
112 suppression for several weeks prior to injection, as we believe that corresponds to the best viral
113 transfection rates.
114

115 ## AAV mediated gene delivery to retina

116 Intravitreal injections were carried out in each animal as previously described [66]. In M1, *7m8-*
117 *SNCG-GCaMP6f* [67] was injected into the right eye; *AAV2-CAG-GCaMP6s* was injected into the
118 left eye of M2 and into the right eye of M3. All vectors were synthesized by the University of
119 Pennsylvania Vector Core. Before the injections, the eyes were sterilized with 50% diluted
120 Betadine, and the vector was injected into the middle of the vitreous at a location approximately
121 4 mm behind the limbus using a tuberculin syringe and 30-gauge needle. Following injection, each
122 eye was imaged with a conventional scanning light ophthalmoscope (Heidelberg Spectralis) using
123 the 488 nm autofluorescence modality to determine onset of GCaMP expression and to
124 periodically monitor image quality and eye health. Animal M1 was injected in March 2017, and
125 data from that animal in this study was taken in March 2019, two years post-injection. Animal
126 M2 was injected in March 2018, and data from that animal in this study was taken in March 2019
127 (1 year post-injection) and July 2019 (1.3 years post-injection). Animal M3 was injected in June
128 2019, and data from that animal in this study was taken in September 2020 (1.25 years post-
129 injection) and in January 2021 (1.5 years post-injection). Efficiency of vector transmission was not
130 explicitly examined in this study and though animal M1 had the lowest mean fluorescence of the

three animals, we cannot meaningfully comment on what percentage of that effect is due to either the lack of immune suppression, post-injection time period, or differences due to the vector used in that animal.

Anesthesia and animal preparation

Anesthesia and animal preparation followed established lab protocols as previously reported [e.g. 16, 68] and were performed by a veterinary technician licensed by the State of New York (USA). All monkeys were fasted overnight prior to anesthesia induction the morning of an imaging session. The animal was placed prone onto a custom stereotaxic cart where it remained for the duration of the imaging session. A Bair Hugger warming system was placed over the animal to maintain body temperature. Monitoring devices including rectal temperature probe, blood pressure cuff, electrocardiogram leads, capnograph, and a pulse oximeter, were used to track vital signs. Temperature, heart rate and rhythm, respirations and end tidal CO_2, blood pressure, SPO_2, and reflexes were monitored consistently and recorded every fifteen minutes. Pupil dilation was accomplished using a combination of Tropicamide 1% and Phenylephrine 2.5%. A full description of all medications used in anesthesia induction, pupil dilation, intubation, and animal recovery can be found in McGregor *et. al.* [68].

Adaptive optics imaging

Data were collected using an AOSLO system previously described in Gray et al. [63]. An updated diagram of the system is shown in S1 Fig. An 847 nm diode laser source (QPhotonics) was used as a beacon for a Shack-Hartmann Wavefront Sensor (SHWS) to measure optical aberrations in each animal's eye in real time, and a Deformable Mirror (ALPAO) was used to correct those aberrations

154 in a closed loop. A 796 nm superluminescent diode source (Superlum) was focused on the
155 photoreceptor layer of the retina to collect reflectance images at an approximately 2 Airy disk
156 confocal pinhole (20 µm), with the images used for both placement of stimuli and later
157 registration (motion correction) of fluorescence images. A 561 nm laser (Toptica) and three LEDs
158 (Thorlabs, center wavelengths 420 nm, 530 nm, 660 nm) were used for visual stimulation of foveal
159 cones. A 488 nm laser source (Qioptiq) was focused on the ganglion cell layer to excite GCaMP
160 fluorescence, which was detected through a 520/35 nm emission filter at an approximately 2 Airy
161 disk confocal pinhole (20 µm) for animals M2 and M3 and an approximately 7.5 Airy disk confocal
162 pinhole (75 µm) for animal M1, each of which was chosen to balance the tradeoff between signal
163 strength and axial resolution. The poorer expression of GCaMP and consequently worse SNR in
164 M1 motivated using the larger confocal pinhole for imaging in that animal. The 488 nm excitation
165 light was presented only during forward scans and filled only the portion of the imaging window
166 where ganglion cells were present to avoid exposing foveal photoreceptors and biasing
167 stimulation. The 488 nm excitation light intensities on the retina were 3.4 mW cm^{-2} in M1, 3.2
168 mW cm^{-2} in M2, and 1.7 mW cm^{-2} in M3, as presented through a dilated pupil size of approximately
169 6.7 mm for each animal. Retinal subtenses were 780 x 570 µm in M1, 765 x 560 µm in M2, and
170 740 x 540 µm or 505 x 380 µm in M3. Imaging sessions using the AOSLO took place starting around
171 9 am and lasted between two to four hours. Room lights were turned off during experiments so
172 that ambient light was minimized and the animal was only exposed to the sources used in the
173 AOSLO. Previous light imaging history was limited to clinical fundus and SLO imaging as mentioned
174 in the AAV mediated gene delivery section.
175

176 **Light safety**

177 The total retinal exposure to all light sources was calculated for each proposed retinal location
178 before each imaging session after measuring the optical power of each source at the pupil plane
179 (sources measured as total optical power across the entire ~6.7 mm pupil: nominally 488 nm at
180 7-15 µW, 561 nm at 5 µW, 796 nm at 250 µW, 847 nm at 30 µW, and combined 5 µW from the
181 LEDs at 420 nm, 530 nm, and 660 nm). For all animals, the total exposure was kept below the
182 maximum permissible exposure for human retina according to the 2014 American National
183 Standards Institute [69-71]. Most exposures were also kept below a reduced ANSI limit that was
184 further scaled by the squared ratio of the numerical aperture of the human eye to the primate
185 eye (~0.78) [72], though imaging sessions in M3 at the smaller FOV exceeded this reduced limit.
186 Imaging sessions were at least five days apart, so accumulated exposure was not taken account
187 into the calculations. According to the ANSI standard, the maximum permissible exposure limit is
188 expressed as a sum of ratios of source powers such that the limit value is unity. In this study,
189 exposures ranged from values of 0.6 – 0.98 corresponding to 60%-98% of the exposure limit.
190

191 Methods to maximize optical quality and signal across experiments

192 The best axial resolution that can be achieved with the confocal AOSLO required for our
193 experiments is 25-30 microns, approximately the diameter of 2-3 RGC somas [27], which means
194 that in areas where the RGC layer is thick, such as the fovea [26, 46], there may be some optical
195 crosstalk from multiple cells contributing to the recorded fluorescence signal. Therefore, as part
196 of the validation of our method and to be certain in describing the physiology of individual cells,
197 we operate in two distinct modalities. The first modality is a wide imaging field of view (FOV) of
198 3.70 x 2.70 deg where we can image hundreds of RGCs across a breadth of soma locations (in M1,
199 M2 and M3), but not be certain that each cell is free of crosstalk. The second modality (only used

200 in M3) is a smaller imaging FOV of 2.54 x 1.92 deg that is centered and focused on the innermost
201 foveal slope, where the RGCs are in a monolayer—in this modality we can only image tens of cells
202 at a time, but we are certain that the signal is not contaminated by optical crosstalk. We present
203 wide field data from all three animals to show cell populations and general physiology, while we
204 present data from the smaller field only from animal M3 to draw conclusions about the physiology
205 of individual cells—the very innermost foveolar RGCs driven by the centermost cones. To ensure
206 the desired imaging FOVs were used in each experiment, the AOSLO system was calibrated using
207 Ronchi gratings of known spacing (80 lp/mm) to translate scanner control voltages into FOV
208 measurements in degrees of visual angle.
209
210 To correct for longitudinal chromatic aberration between the cone reflectance source (796 nm),
211 visual stimulus laser (561 nm), and GCaMP excitation laser (488 nm), the axial source and detector
212 positions of the visible channels were optimized by initial calculation using chromatic dispersion
213 data in humans [73] scaled for the macaque eye. Lateral detector positions were optimized first
214 in a model eye and then further optimized empirically *in vivo* using algorithms such as simplex
215 [74] to iterate over lateral pinhole positions and find the location with maximum detector mean
216 pixel value. For the data in M3 at the inner edge of the foveal slope, an additional experiment
217 optimized the responses of 37 RGCs to 28 c/deg drifting gratings at 6 Hz to find the best axial
218 source position of the 488 nm excitation laser, to account for RGCs on the foveal slope differing
219 in axial position. Transverse chromatic aberration was not critical to stimulus placement in these
220 experiments, but lateral positions of confocal detection pinholes were also optimized using similar
221 algorithms [75].
222

Perhaps as a side effect of the *in vivo* viewing eye being held open for long periods of time during imaging sessions, optical quality tended to degrade over the course of the experiment, slowly at first, but more quickly after the first hour of imaging. To mitigate this, all grating stimuli were presented at the beginning of a session when optical quality was the highest, and only for the first 30 minutes, to minimize degradation of high spatial frequency responses.

Lastly, the isoplanatic patch size of our system is approximately 1-1.5 deg, which is smaller than both of the imaging fields (3.70 x 2.70 deg and 2.54 x 1.92 deg) used in this study. This degrades quality across the entire image and produces field aberrations towards the edges of the images where some ganglion cells were imaged or cones were stimulated. This anisoplanatism, coupled with the fact that the wavefront correction is at a different wavelength than stimulation, means that there could be defocus (see Modeling section) or higher order residual aberrations that preferentially blur high spatial frequency gratings. Care was taken to mitigate or optimize these sources of residual blur, but they cannot completely be eliminated with our current instrument. Therefore, the spatial frequency responses we measured represent a lower bound for the cell responses *in situ* when all sources of residual blur are removed.

Chromatic stimuli

To drive the chromatic responses of RGCs connected to foveal photoreceptors, we presented a 1.3 deg diameter spatially uniform, circular LED stimulus (Thorlabs, center wavelengths and full-widths-at-half-maximums 420±7 nm, 530±17 nm, 660±10 nm) through a Maxwellian view system [76] (S1 Fig). The stimulus was sinusoidally modulated in time. Mean intensities on the retina and temporal frequencies were 6.8 mW cm^{-2} at 0.2 Hz in M1, 7.0 mW cm^{-2} at 0.2 Hz in M2, and 7.6

246 mW cm^{-2} at 0.15 Hz in M3. The slow temporal frequencies were chosen to accommodate the slow
247 temporal response of the GCaMP6 calcium indicator [65] and were adjusted by 0.05 Hz in M3 to
248 avoid potential confound with the respiration rate in that animal. The LED primary wavelengths
249 were chosen to maximize excitation of the L, M, and S cone photopigments [77] while minimizing
250 significant confound by macular pigment absorption [78, 79], the spatial distribution of which was
251 not measured in this study. Each stimulus presentation was 90 s long, following a 30 s adaptation
252 period in which the mean luminance white point and excitation laser were on. The cone
253 fundamentals were constructed using the Govardovskii standard template [80, 81] and the
254 wavelengths of peak absorption for macaque primates [82]. The transmissivity of the eye
255 (including cornea, aqueous, lens, and vitreous) was modeled using measured data from the rhesus
256 macaque [83]. To generate the luminous efficiency function, an equal weighting of the L and M
257 cone fundamentals was used, as the ratio of L and M cones in macaques is close to unity on
258 average [84]. The LEDs were calibrated using a spectrometer (Ocean Optics) validated by a NIST
259 traceable blackbody source. Five silent substitution [85] stimuli were presented at the foveal
260 center while GCaMP responses were recorded. The Psychophysics Toolbox [86] for MATLAB was
261 used to calculate the appropriate power modulations needed: a nominally isoluminant stimulus
262 targeting both L and M cones in counterphase (L modulation 15%, M modulation 17%), an L cone
263 isolating stimulus (24% modulation), an M cone isolating stimulus (33% modulation), an S cone
264 isolating stimulus (92% modulation), and an achromatic luminance stimulus (100% modulation,
265 all cone classes). There was also a control stimulus where the adaptation period was followed by
266 continued presentation of the mean luminance white point. Within one imaging session, each of
267 the stimuli used in that session was presented three times and responses were averaged within
268 the experiment. In M1, only one experiment was performed. In M2 and M3, two experiments
269 across the entire width of soma locations (large imaging FOV) were performed and responses

270 across sessions were averaged. In M3, three separate experiments at the innermost foveal RGCs
271 (small imaging FOV) were performed and averaged.
272

273 Grating stimuli

274 To probe the spatial configuration of foveal RGC receptive fields, we presented monochromatic
275 (561 nm) horizontally-oriented sinusoidal drifting gratings at 6 Hz and 100% contrast. The grating
276 stimuli were presented within the scanned imaging FOV and occupied a square subregion that
277 was either 1.9 deg (large imaging FOV) or 1.3 deg (small imaging FOV) in extent. Mean light
278 intensities on the retina were 1.72 mW cm^{-2} in M2 (large imaging FOV), 1.8 mW cm^{-2} in M3 (large
279 imaging FOV), and 3.2 mW cm^{-2} in M3 (small imaging FOV) imaging only the innermost RGCs
280 closest to the center of the foveola. No data from drifting gratings is shown for animal M1, as the
281 signal was too weak and noisy to produce reliable data from these stimuli. The temporal
282 frequency of these gratings was too fast to allow GCaMP6 to track modulation, so cellular
283 responses were characterized by quantifying the increase in steady fluorescence during
284 stimulation, as opposed to using fluorescence modulation as was done for the slower chromatic
285 stimuli. Grating stimuli were 45 s in duration and were preceded by 15 s adaptation to both the
286 mean luminance of the 561 nm stimulus laser and the 488 nm imaging laser.
287

288 In the small imaging FOV used with M3, the increased resolution meant that the spatial frequency
289 range was 4 c/deg to 49 c/deg. A control (spatially uniform mean luminance) and 14 gratings of
290 different spatial frequency were presented twice each within a session and responses were
291 averaged. Gratings were presented in decreasing order of spatial frequency, to minimize
292 reduction in high spatial frequency response related to decreasing optical quality over the course

293 of the experiment. There were three sessions at the small FOV in M3, and the variability and
294 averages are shown in the results. We note that as gratings were only presented in one
295 orientation, the responses of some cells might be modified by orientation selective effects [87].
296
297 In M2 and M3 at the large imaging FOV, a control and 14 gratings varying in spatial frequency
298 from 2 c/deg to 34 c/deg were presented. Each grating was presented twice within a session and
299 responses were averaged for one session in M2 and across two sessions in M3. These data are
300 not presented in the results because they did not include high enough spatial frequency responses
301 that permit the modeling used in this work (S5 Fig).
302

303 Data analysis

304 To remove blurring and other effects of residual eye movements present in the raw recordings,
305 each video frame of the fluorescence recording was co-registered using corresponding frames
306 from a high signal-to-noise reflectance video of the photoreceptor layer at the same retinal
307 location. During imaging, a reference frame was taken in the reflectance channel to allow for real-
308 time stabilization; this reference frame was also used as the reference for the frame-to-frame
309 cross-correlation method image registration [88] of all videos taken at that location. One
310 registered video, typically one of the videos corresponding to the peak spatial frequency response
311 (usually 10 – 30 cycles/deg), was temporally summed to create a high SNR fluorescence image of
312 the ganglion cell layer, and individual ganglion cells were segmented using the open-source
313 software GIMP. Typically, all identifiable cells in the focal plane were segmented, though cells
314 were excluded if the boundaries between two or more adjacent cells were unclear. The
315 segmentation mask from GIMP was exported to MATLAB, where it was applied to all registered

316 videos at that location to isolate data from individual RGCs. For every frame, the mean of the
317 signal within each cell mask was computed to produce an average signal time course for each cell.
318 When the same stimuli were repeated within a session, the signal time courses for each cell were
319 averaged across all repeated trials.
320
321 For the chromatic data, the temporal speed of the flicker (0.15-0.20 Hz) was well within the
322 temporal resolution of the GCaMP6, thus cells responding to the stimulus exhibited a quasi-
323 sinusoidal modulation in fluorescence level where the amplitude and phase depended on the
324 receptive field properties of the cell and the frequency of the response depended on the stimulus
325 frequency. Each cell's time course was filtered using a Hann windowing function before being
326 Fourier transformed into the frequency domain. The Fourier amplitudes were normalized by
327 subtracting the mean noise at higher frequencies (0.32 Hz - 1.08 Hz) and then dividing by the
328 standard deviation of the noise to produce a response metric equivalent to the sensitivity index
329 d'. The metric was computed for each stimulus for every cell, so that the cells could be plotted in
330 two different configurations from the literature [e.g. 60]. In animals M1 and M2, where an L-M
331 nominally isoluminant stimulus, an S-isolating stimulus, and an achromatic/luminance stimulus
332 were used, no further analysis was needed, and the data was simply plotted along S vs. L-M axes.
333 In animal M3, since single cone isolating stimuli were used for L, M, and S cones, it was possible
334 to reproduce cone weighting plots such as those in Derrington *et. al.* [60]. As in that paper, we
335 calculated the cone weights by dividing the response metric by the cone modulation from the
336 stimuli and normalized them all such that the sum of all cone weights added to unity.
337
338 For the spatial frequency data, the temporal speed of the drifting gratings (6 Hz) exceeded the
339 temporal resolution of the GCaMP6s indicator [65], thus cells responding to the grating exhibited

340 an overall increase in fluorescence that plateaued after approximately 10-20 s. The background
341 level for each cell was calculated as the mean of the first 10 s of fluorescence during the
342 adaptation period, while the signal was calculated as the mean of the last 10 s of fluorescence
343 recorded during the presentation of the stimulus. The ΔF/F metric commonly used in calcium
344 imaging was calculated for each spatial frequency as the background response at that frequency
345 subtracted from the signal at that frequency, all divided by the signal at 17 c/deg, a spatial
346 frequency producing a robust response across the majority of the cells. This function of ΔF/F with
347 respect to spatial frequency is what we refer to as a spatial transfer function (STF) for each RGC
348 measured. An error metric was also calculated for each ΔF/F measurement by using the partial
349 differential error propagation formula using variances [89] and the measured variances in the
350 background response, the signal response, and the signal at 17 c/deg.
351

352 Modeling of photoreceptor mosaic and RGC response 353 characteristics

354 To connect the measured spatial transfer functions (STFs) to the receptive field (RF) organization
355 of the underlying RGCs, we employed a computational model that simulates optical, spectral,
356 spatial, and temporal components of the AOSLO stimulation apparatus, as well as the animal's
357 optics and cone mosaic structure. The model computed cone mosaic responses to simulations of
358 the stimuli used to measure the STF and derived an STF model fit for the RGC under study. The
359 model assumed that cone signals are pooled linearly and instantaneously (ignoring temporal
360 pooling dynamics) by center and surround mechanisms of an RGC according to a difference of
361 Gaussians (DoG) [90] spatial profile. The parameters of the DoG (and therefore the cone pooling
362 weights) were estimated by minimizing the error between the model STF and the measured *in*

363 *vivo* fluorescence-based STF. A model scenario where the center mechanism's Gaussian weighting
364 was replaced by center weighting on just a single cone was also considered. The modeling pipeline
365 depicted schematically in the results, was implemented within the Imaging Systems Engineering
366 Tools for Biology (ISETBio) software framework [91, 92].
367
368 The drifting monochromatic sinusoidal gratings used to measure RGC STFs via the AOSLO
369 apparatus were modeled as temporal sequences of ISETBio spatial-spectral radiance scenes,
370 where each scene models one frame of the displayed stimulus. The spectral characteristics, spatial
371 extent, and the temporal properties of the AOSLO display subsystem were taken into account in
372 generating the ISETBio scenes. The spectral profile of the monochromatic beam was modeled as
373 Gaussian shaped with a peak at 561 nm and a full-width-half-max (FWHM) of 5 nm with a mean
374 irradiance on the retina of 1.29 mW cm^{-2}. The power estimate included absorption by the lens
375 pigment. The visual stimulus as imaged on the retina had a pixel size of 1.03 µm (0.005 deg) with
376 spatial extent 140 x 140 µm (0.7 x 0.7 deg). All sinusoidal gratings were modeled with a nominal
377 contrast of 1.0, drifting at 6 Hz with a refresh rate of 25.3 Hz for a duration of 666 ms (4 cycles).
378
379 The animal's optics during AOSLO-based stimulation were modeled as a diffraction-limited optical
380 system with a small amount of residual defocus blur. The diffraction limit was obtained using the
381 6.7 mm pupil diameter employed in the experiment, assuming a conversion between degrees of
382 visual angle and retinal extent of 199 µm/deg (calculated using the ratio of the axial length of M3
383 16.56 mm to the model human 24.2 mm multiplied by the model human conversion of 291.2
384 µm/deg). Residual blur in the AOSLO, which might occur due to a slight defocus of the stimulus
385 with respect to the plane of cone inner segments in the retina, was modeled by adjusting the
386 Zernike defocus coefficient used to compute the optical point spread function. Residual blur could

also be generated by any other aberrations in the system, imperfect AO correction, or other sources, so the Zernike defocus coefficient was used as a proxy for all sources of residual blur. The amount of residual blur was not known *a priori* and was estimated as part of model fitting as described below. The temporal sequence of ISETBio spatial-spectral radiance scenes that model the AOSLO stimulus were passed via the simulated optical system to generate a corresponding sequence of spatial-spectral retinal irradiance images, which were processed by the cone mosaic model as described next.

An ISETBio model of the animal's cone mosaic was generated from cone density maps measured during AOSLO imaging, using an iterative algorithm described previously [91]. The spatial extent of the modeled cone mosaic was 1.3 x 1.3 deg, with a maximal cone density of 270,200 cones mm^{-2} with relative L:M:S cone densities of 0.48:0.48:0.04 (quasi-regular S cone packing, random L and M cone packing), and without a tritanopic (S-cone free) area at the fovea. Cones were modeled with Gaussian entrance apertures with a characteristic radius equal to $0.204 * \sqrt{2} * D$, where *D* is the inner segment diameter measured during AOSLO imaging [10]. In this cone mosaic model, cone outer segment lengths and macular pigment all varied with eccentricity [91], and the cone quantal efficiencies were based on the Stockman-Sharpe (2000) normalized absorbance measurements [93, 94]. The modeled macular pigment density is taken as the human values provided by Stockman *et. al.* (1999) [93] (http://www.cvrl.org/database/text/maclens/macss.htm), and the modeled lens pigment density is for young human subjects (< 20 years) as reported by Pokorny *et. al.* [95].

To compute a cone's excitation, the spatial-spectral irradiance impinging on the retina was first spectrally weighted by the product of macular pigment transmittance and by each cone's spectral

quantal efficiency, subsequently integrated over wavelength, and spatially integrated over the cone's Gaussian aperture. This excitation response was integrated over the temporal duration of each stimulus frame (39.5 ms), to estimate a spatial map of the expected excitation events count $E^j(\omega,t)$, for the j-th cone in the mosaic, at time t, in response to a drifting grating of spatial frequency ω. In these simulations, we did not include Poisson noise in $E^j(\omega,t)$, nor did we introduce positional jitter between the cone mosaic and the retinal stimulus due to fixational eye movements. In the measured AOSLO data, the animals were anesthetized with eye muscles paralyzed, and digital tracking was employed for stimuli, so retinal motion relative to stimuli was minimized.

Assuming that cones are adapted to the mean background irradiance, the spatiotemporal excitation response $E^j(\omega,t)$ was converted to a spatiotemporal modulation response, $R^j(\omega,t)$, by first subtracting the excitation of the cone to the background stimulus E_0^j, and then dividing by it separately for each cone j, i.e.:

$$R^j(\omega,t) = \frac{E^j(\omega,t) - E_0^j}{E_0^j}$$

This operation captures in broad strokes an important effect of the photocurrent generation process which converts cone absorption events in the inner segment into ionic currents flowing through the cone outer segment, and which in effect down-regulates the stimulus-induced cone excitation rate with respect to the background cone excitation rate.

Model ganglion cell responses $RGC(\omega,t)$, were computed from the cone contrast responses by weighting responses with corresponding center and surround cone weights, followed by spatial pooling within the antagonistic center and surround mechanisms as follows:

$$RGC(\omega,t) = RGC_c(\omega,t) - RGC_s(\omega,t)$$

$$= \sum_j W_c^j * R^j(\omega,t) - \sum_j W_s^j * R^j(\omega,t)$$

where W_c^j and W_s^j are the weights with which the center and surround mechanisms respectively pool the responses $R^j(\omega,t)$. We did not model temporal filtering or delay between center and surround responses. Although real RGC responses may be affected by both temporal filtering and a center-surround delay, measurements in this study only recorded the amplitude of responses at one temporal frequency with no response phase information, so we could not meaningfully estimate temporal RGC parameters.

To make computation of cone weights more tractable, we assumed that the spatial distribution of cone weights to the center and surround mechanisms had concentric, radially-symmetric Gaussian profiles (multi-cone RF center scenario), or that the center drew on a single cone with a Gaussian surround (single-cone RF center scenario):

$$W_c^j = \begin{cases} k_c * \exp\left[-\left(\frac{d_j}{r_c}\right)^2\right] & (multi-cone\ RF\ center\ scenario) \\ k_c & (single-cone\ RF\ center\ scenario) \end{cases}$$

$$W_s^j = k_s * \exp\left[-\left(\frac{d_j}{r_s}\right)^2\right]$$

where d_j is the distance between cone-j and the spatial position of the center mechanism of the model RGC (which is taken as the geometric centroid of the locations of the cones driving the center mechanism). The parameters k_c, k_s, r_c, and r_s, which represent the center and surround peak sensitivities and characteristic radii, respectively, of the DoG RF model were determined by minimizing the root mean squared error (RMSE) between the model-predicted STF, $STF^m(\omega)$, and the measured STF, $STF^{\Delta F/F}(\omega)$, accumulated over all spatial frequencies ω:

$$RMSE = \sqrt{\frac{1}{N} * \sum_{\omega=\omega_1}^{\omega_n} \frac{\beta(\omega)}{\epsilon(\omega)} * [STF^m(\omega) - STF^{\Delta F/F}(\omega)]^2}$$

where ϵ(ω) is the standard error of the mean of the $STF^{\Delta F/F}(\omega)$ measurement, and β(ω) is a high-spatial frequency boost factor which linearly increases with spatial frequency from 0.1 to 1.0 over the spatial frequency range 4.7 to 49 c/deg. This boost factor was introduced to emphasize high spatial frequency measurements, the stimulus regime which is maximally informative about the properties of the center mechanism.

In some cells, and for certain recording sessions, the measured $STF^{\Delta F/F}(\omega)$ dropped below zero for the lowest spatial frequencies. When this occurred, it was accompanied by an apparent overall downward shift in $STF^{\Delta F/F}(\omega)$ across all frequencies, so we assumed that in such cases the background fluorescence was overestimated. To compensate for this, we fit the model to $STF^{\Delta F/F}(\omega) - \min(STF^{\Delta F/F}(\omega))$ instead of $STF^{\Delta F/F}(\omega)$ in cases where $STF^{\Delta F/F}(\omega)$ dropped below zero for any spatial frequency.

To reduce the chance of the minimization algorithm getting stuck at a local minimum of the error function, we employed a multi-start minimizer which was run 512 times, keeping the results from the starting point with the minimum RMSE.

The model-predicted STF, $STF^m(\omega)$, was computed by fitting a sinusoidal function to $RGC^m(\omega, t)$,

$$A(\omega) * \sin[2\pi f t - \theta]$$

where f is set to the temporal frequency of the drifting gratings, and θ, A(ω) are free parameters. At each spatial frequency, the amplitude of the fitted sinusoid, A(ω), was taken as $STF^m(\omega)$.

To interpret the measured STFs, we considered four different model scenarios: single cone RF centers with and without residual defocus in the AOSLO apparatus, and multiple cone RF centers with Gaussian weighting, with and without AOSLO residual defocus. For each scenario, the model was fit to the STF data of an examined RGC at multiple positions within the model cone mosaic and the final model was selected as the one with the minimum RMSE over the examined positions. The multi-position model fitting/selection was performed to take into account local inhomogeneities of the cone mosaic as exact RF center of each recorded RGC is only known to reside approximately within the central 40 microns. Details of the model fitting differences between each scenario, model training, and comparisons between the modeled cone mosaic and the measured mosaic from M3 are provided in S7-S10 Figs. All figures in the main body of the paper assume the single cone center with fixed residual 0.067 D defocus scenario, unless otherwise noted.

Results

In vivo functional imaging of foveal RGCs

In this study, optical stimulation of foveal cones elicits the activity of retinal ganglion cells in the living macaque eye. Intravitreal injection of an adeno-associated virus (7m8 or AAV2) with a promoter (ubiquitous CAG or RGC-specific) produced expression of the calcium indicator GCaMP6f [65] in animal M1 and GCaMP6s [65] in animals M2 and M3. As previously reported, injections in all three animals produced expression in a ring of RGCs surrounding and radiating out from the foveal avascular zone where the internal limiting membrane is thin [66, 68, 96] (Fig 1a). Stimuli were presented to the centermost foveal cones while a 488 nm imaging laser stimulated

500 fluorescence from GCaMP expressing RGCs in a rectangular area placed either nasally or
501 temporally relative to the cones. Fig 2a-b show the fluorescence response of a single RGC to a
502 simple luminance flicker stimulus in time as well as the resulting Fourier transform, which shows
503 the cell responding primarily at the stimulus frequency. Fig 2c shows that, under our stimulus
504 paradigm, the imaging light did not stimulate foveal cones and confound the recorded functional
505 responses after a 561 nm adapting light was presented to the foveal cones. In each animal,
506 hundreds of RGCs were recorded simultaneously using this paradigm, and we used the precision
507 of the AOSLO system to return to the same cells over multiple sessions spanning weeks to months.
508 For examples of the raw time course responses of cells and the variability of responses to
509 individual stimuli across experiments, see S2 and S3 Figs.
510
511 **Fig 1. Stimulus presentation and recording paradigm.** In **(a)** the general stimulation paradigm is
512 shown. Background is an image of the retina of M3 using the blue reflectance imaging modality
513 of a Heidelberg Spectralis instrument. In false color green are GCaMP-expressing cells from M3
514 imaged using the blue autofluorescence modality of the same Spectralis instrument. When using
515 the AOSLO instrument, videos are captured within a rectangular field of view (white dashed line)
516 while stimuli (white circle) such as cone-isolating flicker or drifting gratings (which were
517 rectangular in shape and covered approximately the same area as the white circle) are presented
518 to and centered on the centermost foveal cone photoreceptors. A 488 nm imaging laser in the
519 AOSLO (blue rectangle) excites GCaMP-mediated fluorescent responses of ganglion cells
520 surrounding the foveal slope. **(b)** shows the recorded cone densities at the fovea of M3 and **(c)**
521 shows the ganglion cells segmented (green) at the innermost edge of the foveal slope in M3.
522

523 **Fig 2. Data collection from ganglion cells *in vivo*. (a)** shows the smoothed time course of a single
524 RGC fluorescence response to a 0.15 Hz luminance flicker stimulus. **(b)** shows the amplitude of
525 the Fourier transform of the response time course, recovering the response peak at the stimulus
526 frequency of 0.15 Hz (red dashed line). **(c)** shows the effect of the imaging light on cone-mediated
527 response to stimuli in 62 foveal RGCs. The 488 nm imaging laser which excites GCaMP
528 fluorescence can scatter to foveal cones and confound cone stimulation. If the imaging light is
529 turned on without adaptation to any light, there is a quick rise and slow falloff in fluorescence due
530 to cone responses feeding RGCs. However, if the 561 nm stimulus laser (used for drifting gratings)
531 or LED white point (used for chromatic stimuli) is presented at a mean power of 2-2.5 µW during
532 a short 30s adaptation period prior to imaging onset, then there is no corresponding effect of the
533 imaging light confounding the fluorescence signal. In all recordings, an adaptation light preceded
534 each recording to prevent this transient effect of scattered light from the imaging laser.
535

536 Reliability and precision of foveal RGC recordings

537 Across multiple sessions, RGC somas were recorded from over a range of soma locations between
538 1.2 and 3.5 degrees from the center of the foveal avascular zone (FAZ). When averaging data
539 across multiple experiments, only cells that were visible in all experiments were used. In M3, a
540 follow-up experiment examining only cone density (Fig 1b) found the center of the FAZ to be
541 roughly 41 microns inferior and 51 microns nasal from the peak cone density which agrees with
542 the range of data reported from humans [14]. Based on detailed receptive field mapping
543 performed by McGregor *et. al.* [16], the cones driving the receptive fields of the cells examined in
544 all three animals are likely to be located at eccentricities less than 36 arcmin from the foveal
545 center, or a retinal radius of 120 microns calculated using the primate model eye [97] with the

546 axial lengths of each animal (M1: 17.51 mm, M2: 17.20 mm, M3: 16.56 mm). According to the
547 same mapping, the receptive fields of the innermost cells we recorded from in M3 (Fig 1c) are
548 likely to be driven by cones found at eccentricities less than 6 arcmin, or a retinal radius of 20
549 microns calculated using the same primate model eye and the axial length of M3 (16.56 mm). All
550 visual stimuli delivered to foveal cones were large enough to cover both the FAZ center and the
551 location of maximum cone density and were some 10-60% larger than the cone area servicing
552 even the furthest cells we recorded from, ensuring the best possible chance of recording
553 responses from the maximum number of RGCs.
554

555 Chromatic tuning of foveal RGCs

556 For functional classification of RGCs with receptive fields at the foveal center, chromatic tuning
557 was measured across multiple imaging sessions. Amplitude and phase responses (Fig 3a-d) to
558 spatially uniform 0.15 Hz or 0.20 Hz flicker modulations that were directed along a combination
559 of L, M, L-M, S, and achromatic/luminance directions in color space enabled reliable identification
560 of chromatic tuning of RGCs in all three animals. For each cell, the raw fluorescence time course
561 was measured in response to each visual stimulus, and the Fourier transform was used to find the
562 cell's response amplitude at the stimulus frequency. The signal-to-noise (SNR) response metric
563 was calculated as the response Fourier amplitude (signal) minus the mean amplitudes of higher
564 spatial frequencies (noise), all divided by the standard deviation of the noise. This analysis
565 revealed several functional groups including L-M and M-L opponent cells, S-ON and S-OFF cells,
566 ON and OFF luminance cells, and cells with mixed L vs. M ± S responses. In M3, single cone
567 isolating stimuli were presented to the fovea and the individual cone weights feeding RGCs were
568 calculated as was done previously in LGN [60] (Fig 4a-b). This analysis estimates the relative

569 contribution of each cone class to the response of a cell and revealed further diversity of
570 functional groups, including cells with responses to only L or M cones, as well as various S cone
571 connections to cells with either L or M cone input that were not L vs. M opponent. In figures with
572 individual cell labels for putative midget ganglion cells, cells are named according to their
573 suspected center cone (e.g. L1, L2, M1, etc.). The suspected center cone was chosen based on the
574 assumption that the center response would be the larger than the surround, and that midget
575 ganglion cells connect to a single L or M cone in their center; this labeling is merely a convenience
576 and should not be taken as a definitive measurement of the center cones.
577
578 **Fig 3. Chromatic response properties of RGCs from three different animals.** Black dots show
579 luminance only responding cells, red dots show L-M and M-L cone opponent cells, blue dots show
580 S responding cells, while magenta dots show cells that responded to both L-M and S stimuli.
581 Dotted lines show the significance cutoff of SNR = 2 calculated based on cell responses to the
582 control stimulus (see Methods). Cell response is captured by our signal-to-noise metric described
583 in the Methods. Response phases were also calculated but are not directly shown; however,
584 positive SNRs correspond to responses that were in phase with the stimulus (ON response), while
585 negative SNRs correspond to responses that were approximately 180 deg out of phase with the
586 stimulus (OFF response). The luminance axis is perpendicular to the plane shown and is not
587 included for readability and because not all cells responded to the luminance stimulus. Luminance
588 only cells shown in black thus include both ON and OFF cells. In **(a)**, responses from 15 cells in M1
589 are shown after presentation of spatially uniform luminance, L-M isoluminant and S-isolating
590 stimuli at 0.2 Hz. In **(b)**, responses from 126 cells in M2 are shown after presentation of spatially
591 uniform luminance, L-M isoluminant and S-isolating stimuli at 0.2 Hz. In **(c)**, responses from 83
592 cells (a subset of the cells in Fig 4a, does not contain any cells from Fig 3d) in M3 are shown after

593 presentation of spatially uniform luminance, L-isolating, M-isolating, and S-isolating stimuli at 0.15
594 Hz. In **(d)**, responses from 22 cells (a subset of the cells in Fig 4b) serving the very central fovea of
595 M3 are shown after presentation of spatially uniform luminance, L-isolating, M-isolating, and S-
596 isolating stimuli at 0.15 Hz. These cells are closer to the foveal center than any of the cells shown
597 in (c). In **(c-d)**, all stimuli were single-cone isolating, so the L-M axis is calculated from the single
598 cone L-isolating and M-isolating responses and their relative phase.
599
600 **Fig 4. Cone weights of RGCs from M3.** The horizontal axis shows L cone weight, the vertical axis
601 the M cone weight, and the distance from the origin shows the S cone weight where further away
602 from the origin corresponds to less S-cone weighting. In **(a)**, 100 RGCs (a superset of the cells in
603 Fig 3c, does not contain any cells from Fig 4b) were recorded across the entire width of the
604 GCaMP-expressing ring in M3. There were 3 cells that only showed S cone responses, represented
605 by overlapping circles at the origin. There were also 4 L+M and 11 -L-M luminance only cells that
606 are represented by asterisks in the upper right and lower left. Because these cells only responded
607 to the luminance stimulus but not the L-isolating or M-isolating stimulus, the response sign is
608 known but not the exact L or M cone weighting. In **(b)**, 34 cells (a superset of the cells in Fig 3d)
609 at the innermost edge of the foveal slope in M3, served by the centermost foveal cones, were
610 recorded from. No consistent S only responses were observed, and there were 5 L+M and 2 -L-M
611 luminance only cells.
612

613 Identification of foveolar midget RGCs using chromatic tuning

614 Across all three animals, cells with L-M or M-L cone opponent responses (and no response to S-
615 cone stimuli) were identified as putative midget RGCs. There were a large number of these cells

616 as can be seen in Figs 3 and 4: the proportions of these putative midget cells were 44% (95% CI
617 true proportion of 44±17%) of responsive RGCs closest to the fovea (1.2-1.8 deg soma locations)
618 in M3 (small imaging FOV), 33% (95% CI true proportion of 33±9%) of responsive RGCs over the
619 entire measured range in M3 (large imaging FOV), 72% (95% CI true proportion of 72±8%) of
620 responsive RGCs in M2 (large imaging FOV), and 47% (95% CI true proportion of 47±25%) of
621 responsive RGCs in M1. It is expected that midget RGCs comprise some 70-90% of foveal cells [20,
622 51, 98], and the confidence intervals in M1 and M2 contain values in that range. In M3, single
623 cone isolating stimuli were used as detailed in the chromatic stimuli section—it is expected that
624 these stimuli produce lower responses in the classical cone opponent model of midget RGCs by
625 not driving the center and surround in counterphase as would the isoluminant L-M stimulus used
626 in M1 and M2. There were many cells in M3 (an additional 35% of the closest foveal RGCs, and an
627 additional 32% over the entire measured range) with only an L cone response or only an M cone
628 response and no S cone response. It is possible that some of these cells are cone opponent, but
629 that the single cone isolating stimuli produced too small of a response from the antagonistic
630 surround in those cases. Based on this uncertainty, we cannot say for sure whether the observed
631 number of putative midget RGCs in M3 is outside the range of expected values.
632
633 Soma size is a useful anatomical measure for distinguishing more peripheral ganglion cell types
634 and was examined here as a potential correlate with our putative midget RGCs. RGC soma sizes
635 were measured by two different observers (S4 Fig) using different methods, but as others have
636 reported, soma sizes did not exhibit bimodalities near the fovea [46]. Soma size also did not
637 distinguish between functional groups identified by chromatic tuning (Wilcoxon ranksum test, p
638 > 0.1 for comparisons between L-M, S only, luminance only, and L-M/S cells).
639

640 ## Spatial tuning of foveolar putative midget RGCs

641 Spatially patterned drifting gratings were used to probe the spatial frequency response of RGCs
642 and to augment measurements of chromatic tuning (Fig 5). In M3, at the small field of view
643 focused on the innermost RGCs, a control of spatially uniform mean luminance and drifting
644 gratings of fourteen different spatial frequencies (561 nm, 6 Hz, 4-49 c/deg) were used to
645 stimulate foveal cones while the 488 nm imaging light elicited fluorescence from the same GCaMP
646 expressing RGCs shown in Fig 4b. At this temporal frequency, GCaMP could not track modulation,
647 and responding cells exhibited a sustained increase in fluorescence in response to photoreceptor
648 stimulation. A ΔF/F metric was calculated for each cell as the change in fluorescence under
649 stimulation divided by the mean fluorescence in response to a grating of 17 c/deg (a spatial
650 frequency with a robust response across the majority of the cells). Most, but not all of the putative
651 midget RGCs at the foveal center in M3 (Fig 5), which were all identified according to their L-M or
652 M-L cone opponency, showed two salient features when their spatial frequency response
653 functions were measured: a strong low frequency cut, and a peak in the higher spatial frequencies
654 (20-40 c/deg).

655

656 **Fig 5. Spatial frequency responses of putative midget cells.** Fifteen cells in M3 serving the central
657 foveal cones were identified as L-M or M-L opponent (Fig 3d). Each cell is numbered L1-11 or M1-
658 4 based on whether the suspected center cone was an L or M cone. The red points (circles, Week
659 1), blue points (triangles, Week 2), and green points (squares, Week 3) are measurements from
660 three different experiments each one week apart. The solid orange line in each panel is the
661 average response for that particular cell across all three experiments. The vertical axis is a
662 response metric where the mean baseline fluorescence is subtracted from the fluorescence under

663 stimulation and divided by the fluorescence under stimulation at the peak spatial frequency (see
664 Methods). The error bars show the standard error at each data point, which represents the error
665 in obtaining the signal and background needed to calculate the metric. Additional spatial
666 frequency responses of cells from the large imaging FOV (S5 Fig) and non-midget RGCs (S6 Fig)
667 can be found in the supplement.
668

669 Modeling of foveolar midget RGCs

670 Using the ISETBio-based approach described in the Methods and depicted schematically in Fig 6,
671 we derived estimates of the spatial RF organization from the measured STF data under four
672 different model scenarios involving combinations of residual instrument defocus (zero or some
673 residual defocus) and RF center composition (single or multiple cone inputs). Model cone mosaics
674 matched well in both density and cone size with the measured data in M3 along the horizontal
675 and vertical meridians (S7 Fig). Modeling results from one RGC are depicted in Fig 7. Fig 7a shows
676 results from the modeling scenario that assumes a single cone in the RF center and zero residual
677 defocus. Note that this scenario predicts a diffuse surround and that the derived STF does not
678 agree well with the measured STF, resulting in the largest RMSE across the four examined model
679 scenarios. The STFs derived by the remaining three modeling scenarios match the measured STF
680 approximately equally well even though the resulting cone pooling weights differ. The single cone
681 RF center with 0.067 D residual defocus (Fig 7b) results in a more focal surround than would be
682 true if there were no residual defocus. The multi-cone center RF with zero residual defocus (Fig
683 7c) results in a diffuse RF center and a surround that is marginally more diffuse than the center,
684 which is not consistent with known anatomy of foveal midget RFs. Finally, the multi-cone center
685 0.067 D residual defocus scenario (Fig 7d) results in an RF center with heavy input from one cone

686 and very weak input from nearby cones, and a focal surround. This scenario essentially collapses
687 to the single cone center/0.067 D residual defocus scenario. In Fig 7e-f, the single and multi-cone
688 RF center scenario performances are depicted as a function of assumed residual defocus. Note
689 that for the particular cell shown, the minimal error in the single cone center scenario was at
690 0.077 D of residual defocus, and that the multi-cone scenario never performs better than the best
691 single cone scenario at all residual defocus values modeled. Across all cells examined, the best
692 performance for the single cone RF center scenario was obtained for values of residual defocus
693 between 0 D and 0.082 D with a mean value of 0.067 D. The comparison shown for one cell in Fig
694 7e-f is provided for all cells modeled in S9 Fig. In addition, a cross-validation analysis (S8 Fig)
695 similarly suggests that across all cells, the data do not reject the single cone RF center/0.067 D
696 model relative to the multi-cone center models. Therefore, for the remainder of this paper, we
697 use the single cone RF center/0.067 D residual defocus scenario as the vehicle for interpreting the
698 measured STFs.
699
700 **Fig 6. Schematic overview of the ISETBio modeling approach.** To interpret the AOSLO-based STF
701 measurements (Fig 5) in terms of the spatial pooling of cone signals to the measured RGCs we
702 model the spatial, spectral and temporal aspects of the stimulus, the optics, the cone mosaic and
703 the cone pooling within the center and surrounds mechanisms of an RGC using the ISETBio
704 toolbox. **(a)** A frame of the drifting monochromatic grating stimulus which is projected through
705 the AOSLO system to stimulate and measure the GCaMP fluorescence – based spatial transfer
706 function (STF) of RGCs, $STF^{\Delta F/F}(\omega)$ **(b).** The drifting grating is modeled as a temporal sequence of
707 spatial spectral radiance scenes. These scenes model the AOSLO display including a diffraction-
708 limited optical system with a 6.7 mm pupil **(c)** combined with residual defocus in the eye's wave
709 aberrations **(d).** The resulting sequence of retinal irradiance maps are spectrally integrated and

spatially averaged within the apertures of cones in a model of the animal's cone mosaic **(e)**, resulting in a spatiotemporal sequence of cone excitations **(f).** Cone excitations are transformed to cone modulations by first subtracting and subsequently dividing the mean cone excitation level **(g).** Modulation signals from different cones are scaled by the spatial weights with which the RF center and the RF surround mechanism pool cone signals **(h).** The weighted cone signals are subsequently summed **(i)** to compute the temporal response of the model RGC. A sinusoid is fitted to the RGC temporal response **(j)** and the amplitude of the sinusoid is taken as the STF of the model RGC at the stimulus spatial frequency, $STF^{m}(\omega)$. The RMSE between $STF^{m}(\omega)$ and $STF^{\Delta F/F}(\omega)$ **(k)** is minimized using a multi-start solver which optimizes the center and surround peak sensitivity and radius parameters **(l)** of a difference of Gaussians (DoG) RF model **(m).** The model yields the best-fitting cone pooling weights for the RGC.

Fig 7. Model interpretation of measured STF for a single RGC. a-b show single cone center receptive field models with zero and 0.067 D residual defocus respectively. **c-d** show multi cone center receptive field models with zero and 0.067 D residual defocus respectively. In a – d, the first and second columns depict cone pooling weights for the center and surround mechanism, derived by fitting the model STF to the measured STF. The third column depicts the integrated (along the y-axis) center and surround sensitivity profiles, and the fourth column depicts the model-predicted STF (orange lines) together with the measured STF (green disks). **e-f** show single and multi-cone model residual errors for this particular cell with varying levels of residual defocus. The best residual defocus for individual cells in the single cone center receptive field modeled varies slightly, so 0.067 D was chosen as the value optimizing models across all cells measured.

733 Figure 8 depicts the results of the single-cone RF center/0.067 D scenario for four cells from the
734 center of the fovea of M3. These cells were chosen to showcase the model's fitting to slightly
735 different STF shapes and are not necessarily special in any way. Full results of the model fitting to
736 all 15 cells, including fits for all four scenarios examined, can be found in S10 Fig.
737
738 **Fig 8. ISETBio model receptive field estimates for four additional RGCs.** Each row shows the
739 model fits to a different cell's STF using the single cone center/0.067D residual defocus model.
740
741 The ISETBio model expresses the RFs directly in terms of the weights with which they pool signals
742 from cones in the mosaic, and as such is appropriate for comparison with anatomical
743 measurements and with *in vitro* physiological data where the optics of the eye are not in the
744 stimulus light path. In order to compare our data to other *in vivo* data collected in macaque [e.g.
745 9], where the eye's optics form a blurred image of the visual stimulus, we predicted *in vivo* STFs
746 using the cone pooling weights obtained from the single cone RF center/0.067 D residual defocus
747 scenario. To do so, we swapped the AOSLO optics with the animal's (M3) own wavefront
748 aberration optics as measured *in vivo* and assumed a pupil diameter of 2.5 mm. These
749 physiological optics STFs were computed for 100% contrast achromatic sinusoidal gratings, which
750 matched in their spatial and temporal properties the monochromatic gratings used to measure
751 the STFs in the AOSLO. Results of this analysis are displayed in Fig 9, with three example cells
752 shown in Fig 9a. Here, gray disks and black lines depict the AOSLO STF data and corresponding fit
753 of the model for the AOSLO measurement conditions (single cone RF center/0.067 D residual
754 defocus). Red disks depict the STFs computed using the model combined with M3's optics, and
755 red lines depict a simple DoG model fit to the computed STFs, as is typically done in analysis of *in*

vivo data. Note that the STFs predicted under physiological optics differ substantially from the STFs obtained under near diffraction-limited optics: their magnitude is lower, and their shape is less bandpass. They have weaker attenuation at low frequencies and peak at lower spatial frequencies. This is due to the differential effect of the optical modulation transfer function (MTF) to the STF of the center and surround mechanism, as illustrated in Fig 9b. The left panel depicts the STFs of the center (pink) and surround (blue) mechanism of a model RGC under diffraction-limited optics, and the gray disks represent the corresponding overall STF of the cell. The middle panels depict MTFs for three hypothetical physiological optical systems with increasing amounts of Gaussian blur. The physiological STFs that would be obtained under the three MTF conditions are depicted in the right panels of Fig 9b. Note that as the physiological optics become more blurred, the mapped STF becomes less bandpass and its peak shifts towards lower spatial frequencies. This occurs because the difference between center STF and surround STF decreases as the optics become more blurred. Also note the overall decrease in the magnitude of the STF predicted under physiological optics conditions.

Fig 9. Effect of physiological optics on RGC STFs. a. Gray disks depict STF data measured using the AOSLO for three RGCs, and the black lines show the STFs from the ISETBio model fit to these cells. The cone weights from the model fits are used to predict the STF that would be measured under the animal's own physiological optics (as characterized by wavefront-aberration measurements taken during the experiment) with a 2.5 mm pupil. These model-predicted STFs are depicted by the red disks. A simple DoG model is then fitted to the predicted STF data (red line) for comparison to measurements obtained in traditional *in vivo* neurophysiological experiments (e.g. Croner & Kaplan [9]). **b. Demonstration of the effect of physiological optics on the STF.** The left panel depicts the STFs of the RF center and the RF surround of a model RGC as they would be measured

using diffraction-limited optics (pink and blue, respectively), whereas the composite STF is depicted by the gray disks. The middle panels depict the MTFs of three hypothetical physiological optical systems with progressively larger Gaussian point spread functions. The corresponding STFs that would be measured under these physiological optical systems are depicted in the right panels. Note the difference in scale between left y-axis (for the center and surround STFs) and right y-axis (for composite STFs).

To compare our data with published results on midget RGC STFs obtained *in vivo* from outside the central fovea, we fit the DoG model to the synthesized STFs obtained under the animal's optics and we contrasted the DoG parameters derived using the procedure illustrated in Fig 9a to those reported by Croner & Kaplan [9]. Fig 10 shows the characteristic radii of centers and surrounds of data from M3, as predicted with physiological optics, along with data from Croner & Kaplan. Cone characteristic radii as measured in M3 (blue circles) along with those obtained in *Macaca nemestrina* from Packer *et al.* [99] (blue dashed line) are also shown. Using eccentricity dependent optics derived from off-axis wavefront aberration measurements taken by Jaeken and Artal [100] from human subjects, the anatomical cone apertures from Packer *et. al.* were transformed into their visual space counterparts. This transformation was accomplished by convolving the cone aperture by the point spread function at the corresponding eccentricity, and fitting the result with a two-dimensional Gaussian to derive the characteristic radius in visual space. The result of this computation is shown by the blue cyan line in the right panel. The midget RGC center and surround characteristic radii from M3 lie along a reasonable extrapolation from the Croner & Kaplan data, once eccentricity-varying optics and cone aperture size are accounted for. This supports the hypothesis that the midget pathway is specialized to preserve information at the

803 level of the cone photoreceptor mosaic, and that midget RGCs at the foveola transmit high acuity
804 chromatic information from retinal images.
805
806 Fig 11a depicts population data for R_c/R_s, the ratio of center to surround characteristic radii, which
807 typically shows a smaller center size compared to the surround in the Gaussian model and can
808 vary across RGC types. The data of Croner & Kaplan [9], which were obtained from a wide range
809 of eccentricities, are depicted in gray, whereas data from our foveal RGCs are shown in blue
810 (AOSLO optics) and yellow (M3 as predicted for physiological optics). Note that our population of
811 foveal RGCs has a higher mean R_c/R_s ratio (0.32 under AOSLO, 0.45 under M3 optics) than the
812 population of Croner & Kaplan (0.15), which is not surprising since foveal RGCs are expected to
813 have smaller surrounds than peripheral cells [6, 8, 20].
814
815 Fig 11b depicts population data for K_s/K_c, the ratio of surround to center peak sensitivity, a
816 measure of the surround compared to the center strength weighting, where typically it has been
817 found that the surrounds are much weaker than the centers when expressed in terms of peak
818 sensitivity [9]. Again, there is a difference between our foveal cells with mean K_s/K_c values of 0.28
819 under AOSLO optics and 0.11 under M3's optics, whereas the Croner & Kaplan data have a mean
820 of 0.0094. To the extent that the midget RGC data from M3 and the Croner & Kaplan study [9] are
821 comparable, this suggests that the surround strength expressed as a peak sensitivity ratio is
822 stronger at the foveola than at more eccentric locations, supported by the general trend of the
823 K_s/K_c ratio as a function of eccentricity in both the Croner & Kaplan and M3 data.
824
825 Fig 11c provides the surround/center integrated sensitivity ratio, which is essentially the ratio of
826 the total sensitivities (in a volumetric sense) of surrounds and centers. This does not vary with

827 eccentricity in the Croner & Kaplan data [9], as the variation in R_c/R_s and the variation of K_s/K_c
828 counteract each other such that the integrated sensitivity ratio is relatively constant across midget
829 cells. Consistent with this, the integrated sensitivity ratio for M3 predicted for physiological optics
830 conditions is similar to that found in Croner & Kaplan's data (means of 0.71 and 0.54 respectively).
831 Note also the large effect that the optics have on this value, which rises to 3.37 under the
832 measured AOSLO conditions. Overall, this population analysis shows that our foveal RGCs have a
833 large degree of surround antagonism when the receptive field is expressed directly in terms of
834 how the center and surround draw on the cones in the mosaic, but that this antagonism is greatly
835 attenuated under physiological optics viewing conditions, resulting in center/surround structure
836 in our data that is consistent with what has been observed in previous midget RGC studies across
837 a wide range of eccentricities.
838
839 **Fig 10. Comparison to extra-foveal *in vivo* midget RGC data.** Data from M3 model fits are
840 compared with extra-foveal data from Croner & Kaplan [9]. At left, gray circles and squares
841 respectively show center and surround characteristic radii from Croner & Kaplan as a function of
842 eccentricity, while pink circles and green squares show characteristic radii of centers and
843 surrounds from M3 predicted using the ISETBio model with physiological optics accounted for.
844 Light blue dashed line shows cone characteristic radii data from Packer *et. al.* [99], while blue dots
845 represent cone characteristic radii measured in foveal cones of M3. At right, the cone apertures
846 of Packer *et. al.* were transformed to their visual space counterparts using eccentricity dependent
847 optics derived by off-axis wavefront measurements from human subjects from Jaeken & Artal
848 [100] (blue line). The center and surround characteristic radii (pink circles and green squares) from
849 M3 are also projected into visual space and lie along a natural projection of the Croner & Kaplan
850 data.

Fig 11. Relationship between our findings in foveal midget RGCs and findings in midget RGCs from earlier studies. Data from Croner & Kaplan [9] is shown in gray, data from M3 using the ISETBio model and physiological optics is shown in yellow, and data from M3 using the AOSLO optics is shown in blue. **a.** Analysis of Rc/Rs ratio. Left panel: relationship between the Rc/Rs ratio and retinal eccentricity. Right panel: distribution of Rc/Rs. The mean Rc/Rs ratio in the Croner & Kaplan data is 0.15, vs. 0.45 in our foveal RGCs under physiological optics, and 0.32 in our foveal RGCs under AOSLO optics. **b.** Analysis of Ks/Kc ratio. The mean Ks/Kc ratio in the Croner & Kaplan data is 9.4e-3, vs. 1.1e-1 in our foveal RGCs under physiological optics, and 0.28 in our foveal RGCs under AOSLO optics. **c.** Analysis of integrated surround-to-center ratio, (Ks/Kc) x $(Rs/Rc)^2$. The mean integrated surround-to-center ratio in the Croner & Kaplan data is 0.54, vs. 0.71 in our foveal RGCs under physiological optics, and 3.37 in our foveal RGCs under AOSLO optics.

Discussion

In this study, we repeatedly imaged the same RGCs serving the foveal center *in vivo*, in three animals, returning to the same retinal locations each time. Spatially uniform chromatic visual stimuli enabled the identification of L-M and M-L opponent cells which were further interrogated in one animal with drifting gratings of various spatial frequencies. Detailed modeling revealed how the receptive fields of these RGCs draw on the cones of the retinal mosaic. The L vs. M opponency and high spatial frequency responses of these cells identifies them as candidate midget RGCs. Our modelling is consistent with the hypothesis that these cells have single cone center inputs and are specialized to preserve the resolution of the cone photoreceptor mosaic in the signals they send to the visual cortex.

874

875 ## Measuring the precise location of cells from the foveal center

876 In our data, the foveal avascular zone (FAZ) was used as the 'center' measurement of the fovea,
877 as the imaging paradigm precluded using the location of maximum photoreceptor density for all
878 sessions. The preferred retinal locus of fixation (PRL) is also of interest but could not be
879 determined using our method, since the animals are anesthetized during the experiments and
880 cannot freely fixate. The center of the ganglion cell ring surrounding the fovea is also sometimes
881 used to define the center of the fovea, but this measure is highly correlated with the center of the
882 FAZ [11, 101]. A more sophisticated measure of the 'physiological center' can be identified using
883 white noise stimuli as in McGregor *et. al.* [16], but those stimuli were not used in this study. Others
884 have characterized the precise nature of the relationship between these various measures [14],
885 and as noted in the results, our measurements of the difference between the center of the FAZ
886 and the location of maximum cone density in M3 are in agreement with that literature. In any
887 case, the difference in identification of the 'foveal center' is not large enough under our method
888 to affect the conclusion that, using the mapping of McGregor *et. al.* [16], the receptive fields we
889 examined are located near the very center of the foveola.

890

891 ## Comparison of methodology used in this study with traditional
892 ## electrophysiology

893 Functional measurements of RGCs made in the past often involved flashed stimuli and marking
894 approximate estimates of soma location on fundus images of the retina [e.g. 9, 102], a method
895 that leads to uncertainty about precise locations. In contrast, our imaging method captures

896 photoreceptors, vasculature, and RGC somas in the same field of view, allowing more accurate
897 measurements of receptive field eccentricity and soma position. One shortcoming of *in vivo*
898 functional imaging compared to traditional electrophysiology is that the excitation and imaging
899 sources can interfere with stimulation or fluorescence detection. However, unlike in the
900 periphery, foveal RGCs are displaced laterally from their photoreceptor inputs [1, 11, 15, 98].
901 Thus, our paradigm avoids this pitfall, and we can reliably image foveal RGCs without the 488 nm
902 excitation light stimulating foveal cones (Fig 2c) or the photoreceptor stimuli interfering with the
903 RGC GCaMP fluorescence imaging. As mentioned in the Methods, our technique affords the
904 advantage of being able to record from hundreds of cells simultaneously, a feat matched by multi-
905 electrode arrays [e.g. 35, 39, 49, 55, 103-105] but without the same spatial control or ability to
906 view the cells during recording. However, when imaging hundreds of cells from a wide field of
907 view in our technique, there is the possibility of optical crosstalk from cell responses originating
908 from different depths in the ganglion cell layer. Currently, the only way to get around this in our
909 existing system is to use smaller fields of view focused on the foveal slope where ganglion cells
910 are in a monolayer. In the future, methods that improve the axial resolution of *in vivo* imaging,
911 such as combining adaptive optics with optical coherence tomography [e.g. 46, 106-108], will be
912 required to achieve the same level of single-cell specificity that that is achievable with current
913 electrophysiology techniques.
914

915 **S-cone mediated color vision in the fovea**

916 As shown in Figs 3 and 4, cells with either S cone input without L vs. M cone opponency (pure) or
917 S cone input on top of L vs. M opponency (mixed) were observed in each animal. 40% of
918 responsive cells exhibited pure S responses and 7% mixed in M1, 9% pure and 14% mixed in M2,

919 16% pure and 3% mixed in the near fovea of M3 (large imaging FOV), while no consistent S cone
920 responses were recorded from the centermost foveolar cells (small imaging FOV) in M3. Other
921 than in M1 where the sample size was only 15 cells, these numbers are consistent with the
922 expected S cone density of approximately 10% across primate fovea [109] and the known
923 reduction of S cone density at the very center of the primate fovea [8, 15]. Others have reported
924 subtypes of midget RGCs with S cone input or even that midget RGCs may indiscriminately contact
925 S cones along with L and M cones in the surround [4, 17, 48, 110, 111]. Our current data set has
926 no repeatable S cone responses for RGCs at the innermost foveal edge in M3, where RGCs are
927 optically well-isolated, so we cannot rule out that the mixed cells we measure are partially or fully
928 the product of optical crosstalk resulting from the 25-30µm axial resolution of the AOSLO
929 instrument.
930

931 Putative parasol cells at the fovea

932 As shown in Figs 3 and 4, cells with no chromatic responses but only a L+M or -L-M luminance
933 response were recorded from each of the three animals: 7% of responsive cells in M1, 4% in M2,
934 15% in the entirety of M3 and 20% of the centermost foveal cells in M3, consistent with expected
935 proportions of parasol ganglion cells, which are known to mediate achromatic vision [20]. Simple
936 modeling based on hexagonal packing of cones and random wiring of 6 cones to midget surrounds
937 suggests that approximately 9% of midget RGCs could be dominated by a single cone type and
938 appear achromatic (S11 Fig). It is probable then that some of these achromatic cells are midget
939 RGCs but that most of them are candidate parasol cells, though at this time we cannot make that
940 distinction for an individual cell. The spatial frequency response properties of these cells were
941 even more varied than the chromatic opponent cells (S6 Fig), suggesting that they might be

942 responsible for a wide range of achromatic or even temporal vision properties that complement
943 the midget system. As noted in the results, we have not found significant differences between
944 soma sizes of putative foveal parasol and midget RGCs, so additional anatomical information such
945 as histological studies may be required in the future to confirm functional designations.
946

947 The role of midget RGCs in foveal vision

948 Among the putative midget RGCs from M3 (Figs 5 and 7-9), there was some variability among the
949 responses to spatial frequencies in that a subset of cells possessed lower spatial frequency
950 response peaks (0-20 c/deg) compared to the peak spatial frequencies of the majority of the cells
951 (20-40 c/deg), though both of these groups of cells were well fit by the single-cone RF
952 center/0.067 D residual defocus model scenario, suggesting that the change in their peak spatial
953 frequency is related to the surround size and/or ratio of center and surround strengths, as
954 opposed to the spatial extent of the center. Previous studies examining parvocellular neurons in
955 the lateral geniculate nucleus (LGN) serving the central five degrees of retina found an average of
956 4.57±2.75 c/deg as the peak spatial frequency response [62], and other studies in the retina found
957 parvocellular cells in the central five degrees to have a peak spatial frequency response around 3
958 c/deg [9]. However, these previous studies relied on presenting stimuli through the animals'
959 optics, whereas the adaptive optics method we use approaches near diffraction-limited stimulus
960 presentation with some possible residual defocus. Indeed, as shown in Figs 9 and 10, when the
961 animal's optics are added back into a simulation of our data from M3, we recover the classically
962 measured bandpass shape and lower spatial frequency peaks that are expected of parvocellular
963 neurons (midget RGCs). We thus measure putative midget RGCs not only closer to the foveal
964 center and with greater precision than previously achievable, but also with diminished optical blur

965 in the *in vivo* retina compared to previous studies, with the exception of studies that used
966 interferometric stimuli to bypass the optics altogether [e.g. 10]. We thus posit that the
967 parameters of spatial DoG models fit to data collected through the optics do not directly represent
968 the *in situ* characteristics of RGCs, and that future *in vivo* measurements and models need to take
969 into account the effects of diffractive and optical blurring on the measured spatial transfer
970 functions.
971
972 In all 15 L-M and M-L cone opponent RGCs serving the central foveola, we could not reject the
973 hypothesis that the receptive fields were best described by a single cone center with some
974 residual instrumental defocus (0.067 D). There were some cells where the single cone
975 center/0.067 D scenario was clearly the best fit, but for many cells several of the scenarios
976 performed similarly in terms of RMSE—full details for all scenarios can be found in S10 Fig**.** We
977 posit that since the fovea is specialized for high acuity vision, it must be capable of extracting high
978 spatial frequency information from natural scenes which are known to follow a $1/f^2$ law [112] and
979 are dominated by low frequency information. Our modeling that adds the optics of M3 back into
980 the predictions (Fig 9) suggests that natural ocular aberrations reduce the peak spatial frequency
981 obtained under AOSLO conditions by a factor of three or more, which means that high spatial
982 frequency information is greatly reduced by ocular transmission. Thus, to extract meaningful high
983 spatial frequency information from natural scenes through the eye's native optics, detectors that
984 preserve information at the resolution of the cone photoreceptor mosaic are required. It seems
985 highly probable that the putative midget RGCs shown in Figs 5 and 8 are responsible for this
986 resolution, as they have responses consistent with single cone receptive field centers and most
987 have spatial transfer functions that peak well into the 20-40 c/deg range when measured with
988 respect to a retinal image under AOSLO conditions. McMahon *et al.* [10] measured the spatial

989 frequency responses of parvocellular LGN cell centers near the foveola using interference fringes,
990 which are not subject to blur by diffraction. They found that cells still had detectable responses
991 to spatial frequencies above 100 c/deg, with some responses that were complex and inconsistent
992 with a simple difference of Gaussians model. Because the AO-corrected stimuli used in the
993 present study were subject to blur by diffraction, we were unable to explore responses at the high
994 spatial frequencies where such effects were observed.
995
996 Putative midget RGCs with the lowest spatial frequency peaks comprised only 2/15 cells (cells L2
997 and M3) compared to ones with higher spatial frequency peaks (13/15 cells). The two cells with
998 lowest spatial frequency peaks had stronger surround weighting compared to the centers (higher
999 K_s/K_c ratio) coupled with surrounds that were almost spatially coexistent with the centers. These
1000 two cells are inconsistent with previous data finding the center responses of midget RGCs to be
1001 some 10x-1000x stronger than those of the surround and finding centers to be much smaller in
1002 spatial extent than surrounds [9]. The cells with higher spatial frequency peaks had center and
1003 surround strength ratios closer to previous data, though all 15 cells had higher surround/center
1004 integrated sensitivity ratios than previous results such as those reported by Croner & Kaplan [9].
1005 These differences, however, are explainable by the blurring effect of the optics as presented in
1006 Figs 9-11. Further study of low-frequency L-M and M-L cone opponent cells will confirm if they
1007 exhibit any other physiological differences or if they belong to one or more of several midget
1008 subtypes as others have postulated to exist [48, 110]. There is also evidence that parasol ganglion
1009 cells can respond weakly to L vs. M modulation [113], but they are not expected to have single
1010 cone centers from anatomy [6, 20, 27, 114], so it is unlikely that any of the 15 cells studied here
1011 are parasols.
1012

Modeling foveolar RGCs

In our modeling, we could not reject the hypothesis that the 15 cells studied from the center of the fovea in M3 had single cone centers with some residual optical blur, beyond diffraction, present in the measurements. We think it likely that there was some residual optical blur, and certainly cannot reject this idea. However, we note that model scenarios that did not restrict to a single-cone center also describe the data, and that if no residual blur is assumed then the single-cone center model can be rejected for some cells. There are two reasons it is difficult to differentiate between single and multi-cone scenarios from our data. First, due to limitations imposed by the pixel density of the raster scan, our measurements did not extend to high spatial frequencies (>50 c/deg) where the different scenarios would make more clearly different predictions. Second, there was inter-session variability in the measured STFs (Fig 5), which decreases the power of the data. In future experiments, we plan to (i) extend the range of spatial frequencies examined and (ii) test multiple grating orientations. Despite these limitations, as noted in S10 Fig, the multi-cone RF scenario with residual defocus often produces a RF strikingly similar to the single-cone RF scenario with residual defocus, with only a minimal amount of cone coupling, and the classical understanding of midget RGCs that postulates single-cone centers is consistent with our data.

A notable observation of the STFs in our population of foveal RGCs (Fig 8) is the large amount of low-spatial frequency attenuation. Such observations are not typical of midget ganglion cells reported in other *in vivo* studies [9]. The question then arises as to whether these most central foveal cells have distinctively different RF organization from the less-foveal cells reported in other studies, or whether the underlying RF organization is similar, but the measured data differ between the two types of studies simply because of differences in the optical systems involved.

When the animal's optics are added back in (Figs 9-11), the STFs have a clear shift of peak sensitivity towards lower spatial frequencies, approaching those of previous *in vivo* studies but not exactly replicating them, suggesting that the optics account for most of the observed differences with the possibility of modest foveal specialization or instrument differences accounting for the rest.

The modeling used in this study has the capability to add a subject's optical point spread function (here through the measured wavefront aberrations from M3) to predict responses to stimuli presented through the natural (non-AO-corrected) optics. The robust nature of the entire simulation allows for any cone density profile or PSF to be substituted in the model so that the simulation can be generalized to population data or be tailored to individual subjects, as it has been here for M3.

Conclusions

In this study, measurements of chromatic and spatial properties were repeated for hundreds of foveal retinal ganglion cells across three macaque animals. Cells with S cone responses were found in proportions consistent with known S cone density at the fovea, as were achromatic cells found in proportions consistent with known parasol RGC densities. Putative midget RGCs at the center of the foveola were identified by their unique L vs. M cone opponency and had spatial responses consistent with single cone centers. Two out of fifteen RGCs with L vs. M opponency were identified as being inconsistent with the established view of midget cells, in that although their responses were consistent with single cone centers, they have extremely strong surround opponency that is almost spatially coextensive with the centers. In general, the putative midget

1060 cells were consistent with measured responses from outside the fovea when the blurring effect
1061 of diffraction and the animals' optics was taken into account. Spatial frequency response
1062 measurements made using adaptive optics are closer to the *in situ* properties of RGCs than other
1063 *in vivo* methods as shown by our modeling, and future models of retinal neurons will need to take
1064 into account the effect of optical blurring on spatial transfer functions to connect the *in situ*
1065 properties to the cell's function for natural viewing.
1066

1067 # Acknowledgments

1068 The authors would like to thank Amber Walker for performing animal anesthesia and monitoring
1069 during imaging, Deniz Dalkara for providing the viral vector used in M1, Max Snodderly for
1070 assistance with estimating the effect of macular pigment, Charles Granger for optical alignment
1071 assistance, Daniel Guarino and Martin Gira for maintaining the stereotaxic cart and other
1072 electronic components, as well as Aby Joseph, Jennifer Hunter, and Jesse Schallek for data analysis
1073 suggestions. We thank the vector core at the Perelman School of Medicine, University of
1074 Pennsylvania and the Genetically-Encoded Neuronal Indicator and Effector (GENIE) Project and
1075 the Janelia Research Campus of the Howard Hughes Medical Institute, specifically Vivek
1076 Jayaraman, Ph.D., Douglas S. Kim, Ph.D., Loren L. Looger, Ph.D., and Karel Svoboda, Ph.D.
1077

1078 # References

1079 1. Schein SJ. Anatomy of macaque fovea and spatial densities of neurons in foveal
1080 representation. J Comp Neurol. 1988;269(4):479-505. Epub 1988/03/22. doi:
1081 10.1002/cne.902690403. PubMed PMID: 3372725.
1082 2. Wassle H, Grunert U, Rohrenbeck J, Boycott BB. Cortical magnification factor and the
1083 ganglion cell density of the primate retina. Nature. 1989;341(6243):643-6. Epub 1989/10/19.
1084 doi: 10.1038/341643a0. PubMed PMID: 2797190.

1085 3. Wassle H, Grunert U, Rohrenbeck J, Boycott BB. Retinal ganglion cell density and cortical
1086 magnification factor in the primate. Vision Res. 1990;30(11):1897-911. Epub 1990/01/01.
1087 PubMed PMID: 2288097.
1088 4. De Monasterio FM, Gouras P. Functional properties of ganglion cells of the rhesus
1089 monkey retina. J Physiol. 1975;251(1):167-95. Epub 1975/09/01. doi:
1090 10.1113/jphysiol.1975.sp011086. PubMed PMID: 810576; PubMed Central PMCID:
1091 PMCPMC1348381.
1092 5. Derrington AM, Lennie P. Spatial and temporal contrast sensitivities of neurones in
1093 lateral geniculate nucleus of macaque. J Physiol. 1984;357:219-40. Epub 1984/12/01. doi:
1094 10.1113/jphysiol.1984.sp015498. PubMed PMID: 6512690; PubMed Central PMCID:
1095 PMCPMC1193256.
1096 6. Watanabe M, Rodieck RW. Parasol and midget ganglion cells of the primate retina. J
1097 Comp Neurol. 1989;289(3):434-54. Epub 1989/11/15. doi: 10.1002/cne.902890308. PubMed
1098 PMID: 2808778.
1099 7. Kolb H, Dekorver L. Midget ganglion cells of the parafovea of the human retina: a study
1100 by electron microscopy and serial section reconstructions. J Comp Neurol. 1991;303(4):617-36.
1101 Epub 1991/01/22. doi: 10.1002/cne.903030408. PubMed PMID: 1707423.
1102 8. Hendrickson A. A morphological comparison of foveal development in man and monkey.
1103 Eye (Lond). 1992;6 (Pt 2):136-44. Epub 1992/01/01. doi: 10.1038/eye.1992.29. PubMed PMID:
1104 1624035.
1105 9. Croner LJ, Kaplan E. Receptive fields of P and M ganglion cells across the primate retina.
1106 Vision Res. 1995;35(1):7-24. Epub 1995/01/01. doi: 10.1016/0042-6989(94)e0066-t. PubMed
1107 PMID: 7839612.
1108 10. McMahon MJ, Lankheet MJ, Lennie P, Williams DR. Fine structure of parvocellular
1109 receptive fields in the primate fovea revealed by laser interferometry. J Neurosci.
1110 2000;20(5):2043-53. Epub 2000/02/24. PubMed PMID: 10684905.
1111 11. Hendrickson A. Organization of the Adult Primate Fovea. In: Penfold PL, Provis JM,
1112 editors. Macular Degeneration: Springer Berlin Heidelberg; 2005.
1113 12. Yin L, Masella B, Dalkara D, Zhang J, Flannery JG, Schaffer DV, et al. Imaging light
1114 responses of foveal ganglion cells in the living macaque eye. J Neurosci. 2014;34(19):6596-605.
1115 Epub 2014/05/09. doi: 10.1523/jneurosci.4438-13.2014. PubMed PMID: 24806684; PubMed
1116 Central PMCID: PMCPMC4012315.
1117 13. Sinha R, Hoon M, Baudin J, Okawa H, Wong ROL, Rieke F. Cellular and Circuit
1118 Mechanisms Shaping the Perceptual Properties of the Primate Fovea. Cell. 2017;168(3):413-
1119 26.e12. Epub 2017/01/28. doi: 10.1016/j.cell.2017.01.005. PubMed PMID: 28129540; PubMed
1120 Central PMCID: PMCPMC5298833.
1121 14. Wilk MA, Dubis AM, Cooper RF, Summerfelt P, Dubra A, Carroll J. Assessing the spatial
1122 relationship between fixation and foveal specializations. Vision Research. 2017;132:53-61. doi:
1123 https://doi.org/10.1016/j.visres.2016.05.001.
1124 15. Bringmann A, Syrbe S, Gorner K, Kacza J, Francke M, Wiedemann P, et al. The primate
1125 fovea: Structure, function and development. Prog Retin Eye Res. 2018;66:49-84. Epub
1126 2018/04/03. doi: 10.1016/j.preteyeres.2018.03.006. PubMed PMID: 29609042.
1127 16. McGregor JE, Yin L, Yang Q, Godat T, Huynh KT, Zhang J, et al. Functional architecture of
1128 the foveola revealed in the living primate. PLoS One. 2018;13(11):e0207102. Epub 2018/11/30.
1129 doi: 10.1371/journal.pone.0207102. PubMed PMID: 30485298; PubMed Central PMCID:
1130 PMCPMC6261564.

1131 17. Thoreson WB, Dacey DM. Diverse Cell Types, Circuits, and Mechanisms for Color Vision
1132 in the Vertebrate Retina. Physiol Rev. 2019;99(3):1527-73. Epub 2019/05/30. doi:
1133 10.1152/physrev.00027.2018. PubMed PMID: 31140374; PubMed Central PMCID:
1134 PMCPMC6689740.
1135 18. Dacey DM. The mosaic of midget ganglion cells in the human retina. J Neurosci.
1136 1993;13(12):5334-55. Epub 1993/12/01. PubMed PMID: 8254378.
1137 19. Dacey DM. Primate retina: cell types, circuits and color opponency. Prog Retin Eye Res.
1138 1999;18(6):737-63. Epub 1999/10/26. doi: 10.1016/s1350-9462(98)00013-5. PubMed PMID:
1139 10530750.
1140 20. Dacey DM. Origins of Perception: Retinal Ganglion Cell Diversity and the Creation of
1141 Parallel Visual Pathways. In: Gazzaniga MS, editor. The Cognitive Neurosciences: The MIT Press;
1142 2004. p. 281-302.
1143 21. Hansen T, Pracejus L, Gegenfurtner KR. Color perception in the intermediate periphery
1144 of the visual field. J Vis. 2009;9(4):26.1-12. Epub 2009/09/18. doi: 10.1167/9.4.26. PubMed
1145 PMID: 19757935.
1146 22. Leventhal AG, Rodieck RW, Dreher B. Retinal ganglion cell classes in the Old World
1147 monkey: morphology and central projections. Science. 1981;213(4512):1139-42. Epub
1148 1981/09/04. doi: 10.1126/science.7268423. PubMed PMID: 7268423.
1149 23. Perry VH, Cowey A. Retinal ganglion cells that project to the superior colliculus and
1150 pretectum in the macaque monkey. Neuroscience. 1984;12(4):1125-37. Epub 1984/08/01. doi:
1151 10.1016/0306-4522(84)90007-1. PubMed PMID: 6483194.
1152 24. Perry VH, Oehler R, Cowey A. Retinal ganglion cells that project to the dorsal lateral
1153 geniculate nucleus in the macaque monkey. Neuroscience. 1984;12(4):1101-23. Epub
1154 1984/08/01. doi: 10.1016/0306-4522(84)90006-x. PubMed PMID: 6483193.
1155 25. Kaplan E, Shapley RM. The primate retina contains two types of ganglion cells, with high
1156 and low contrast sensitivity. Proceedings of the National Academy of Sciences of the United
1157 States of America. 1986;83(8):2755-7. Epub 1986/04/01. doi: 10.1073/pnas.83.8.2755. PubMed
1158 PMID: 3458235; PubMed Central PMCID: PMCPMC323379.
1159 26. Perry VH, Silveira LCL. Functional lamination in the ganglion cell layer of the macaque's
1160 retina. Neuroscience. 1988;25(1):217-23. doi: https://doi.org/10.1016/0306-4522(88)90020-6.
1161 27. Dacey DM, Petersen MR. Dendritic field size and morphology of midget and parasol
1162 ganglion cells of the human retina. Proceedings of the National Academy of Sciences of the
1163 United States of America. 1992;89(20):9666-70. doi: 10.1073/pnas.89.20.9666. PubMed PMID:
1164 1409680.
1165 28. Grunert U, Greferath U, Boycott BB, Wassle H. Parasol (P alpha) ganglion-cells of the
1166 primate fovea: immunocytochemical staining with antibodies against GABAA-receptors. Vision
1167 Res. 1993;33(1):1-14. Epub 1993/01/01. PubMed PMID: 8383899.
1168 29. Dacey DM. Morphology of a small-field bistratified ganglion cell type in the macaque
1169 and human retina. Vis Neurosci. 1993;10(6):1081-98. Epub 1993/11/01. doi:
1170 10.1017/s0952523800010191. PubMed PMID: 8257665.
1171 30. Dacey DM, Lee BB. The 'blue-on' opponent pathway in primate retina originates from a
1172 distinct bistratified ganglion cell type. Nature. 1994;367(6465):731-5. Epub 1994/02/24. doi:
1173 10.1038/367731a0. PubMed PMID: 8107868.
1174 31. Graham DM, Wong KY. Melanopsin-expressing, Intrinsically Photosensitive Retinal
1175 Ganglion Cells (ipRGCs). In: Kolb H, Fernandez E, Nelson R, editors. Webvision: The Organization
1176 of the Retina and Visual System. Salt Lake City (UT)1995.

1177 32. Dacey DM. Circuitry for color coding in the primate retina. Proceedings of the National
1178 Academy of Sciences of the United States of America. 1996;93(2):582-8. Epub 1996/01/23. doi:
1179 10.1073/pnas.93.2.582. PubMed PMID: 8570599; PubMed Central PMCID: PMCPMC40095.
1180 33. Lee BB. Receptive field structure in the primate retina. Vision Research. 1996;36(5):631-
1181 44. doi: https://doi.org/10.1016/0042-6989(95)00167-0.
1182 34. Calkins DJ, Tsukamoto Y, Sterling P. Microcircuitry and mosaic of a blue-yellow ganglion
1183 cell in the primate retina. J Neurosci. 1998;18(9):3373-85. Epub 1998/05/09. PubMed PMID:
1184 9547245; PubMed Central PMCID: PMCPMC6792640.
1185 35. Chichilnisky EJ, Baylor DA. Receptive-field microstructure of blue-yellow ganglion cells in
1186 primate retina. Nat Neurosci. 1999;2(10):889-93. Epub 1999/09/24. doi: 10.1038/13189.
1187 PubMed PMID: 10491609.
1188 36. Telkes I, Distler C, Hoffmann KP. Retinal ganglion cells projecting to the nucleus of the
1189 optic tract and the dorsal terminal nucleus of the accessory optic system in macaque monkeys.
1190 Eur J Neurosci. 2000;12(7):2367-75. Epub 2000/08/18. doi: 10.1046/j.1460-9568.2000.00133.x.
1191 PubMed PMID: 10947815.
1192 37. Dacey DM, Liao HW, Peterson BB, Robinson FR, Smith VC, Pokorny J, et al. Melanopsin-
1193 expressing ganglion cells in primate retina signal colour and irradiance and project to the LGN.
1194 Nature. 2005;433(7027):749-54. Epub 2005/02/18. doi: 10.1038/nature03387. PubMed PMID:
1195 15716953.
1196 38. Calkins DJ, Sterling P. Microcircuitry for two types of achromatic ganglion cell in primate
1197 fovea. J Neurosci. 2007;27(10):2646-53. Epub 2007/03/09. doi: 10.1523/JNEUROSCI.4739-
1198 06.2007. PubMed PMID: 17344402; PubMed Central PMCID: PMCPMC6672494.
1199 39. Petrusca D, Grivich MI, Sher A, Field GD, Gauthier JL, Greschner M, et al. Identification
1200 and characterization of a Y-like primate retinal ganglion cell type. J Neurosci.
1201 2007;27(41):11019-27. Epub 2007/10/12. doi: 10.1523/jneurosci.2836-07.2007. PubMed PMID:
1202 17928443.
1203 40. Field GD, Sher A, Gauthier JL, Greschner M, Shlens J, Litke AM, et al. Spatial Properties
1204 and Functional Organization of Small Bistratified Ganglion Cells in Primate Retina. The Journal of
1205 Neuroscience. 2007;27(48):13261-72. doi: 10.1523/jneurosci.3437-07.2007.
1206 41. Crook JD, Peterson BB, Packer OS, Robinson FR, Gamlin PD, Troy JB, et al. The smooth
1207 monostratified ganglion cell: evidence for spatial diversity in the Y-cell pathway to the lateral
1208 geniculate nucleus and superior colliculus in the macaque monkey. J Neurosci.
1209 2008;28(48):12654-71. Epub 2008/11/28. doi: 10.1523/jneurosci.2986-08.2008. PubMed PMID:
1210 19036959; PubMed Central PMCID: PMCPMC2778055.
1211 42. Percival KA, Martin PR, Grunert U. Organisation of koniocellular-projecting ganglion cells
1212 and diffuse bipolar cells in the primate fovea. Eur J Neurosci. 2013;37(7):1072-89. Epub
1213 2013/01/15. doi: 10.1111/ejn.12117. PubMed PMID: 23311464.
1214 43. Crook JD, Packer OS, Troy JB, Dacey DM. Synaptic Mechanisms of Color and Luminance
1215 Coding: Rediscovering the X-Y-cell dichotomy in primate retinal ganglion cels. . In: Werner JS,
1216 Chalupa LM, editors. The New Visual Neurosciences: The MIT Press; 2013. p. 123-44.
1217 44. Puller C, Manookin MB, Neitz J, Rieke F, Neitz M. Broad thorny ganglion cells: a
1218 candidate for visual pursuit error signaling in the primate retina. J Neurosci. 2015;35(13):5397-
1219 408. Epub 2015/04/04. doi: 10.1523/jneurosci.4369-14.2015. PubMed PMID: 25834063;
1220 PubMed Central PMCID: PMCPMC4381007.
1221 45. Liao HW, Ren X, Peterson BB, Marshak DW, Yau KW, Gamlin PD, et al. Melanopsin-
1222 expressing ganglion cells on macaque and human retinas form two morphologically distinct

1223 populations. J Comp Neurol. 2016;524(14):2845-72. Epub 2016/03/15. doi: 10.1002/cne.23995.
1224 PubMed PMID: 26972791; PubMed Central PMCID: PMCPMC4970949.
1225 46. Liu Z, Kurokawa K, Zhang F, Lee JJ, Miller DT. Imaging and quantifying ganglion cells and
1226 other transparent neurons in the living human retina. Proceedings of the National Academy of
1227 Sciences of the United States of America. 2017;114(48):12803-8. Epub 2017/11/16. doi:
1228 10.1073/pnas.1711734114. PubMed PMID: 29138314; PubMed Central PMCID:
1229 PMCPMC5715765.
1230 47. Peng YR, Shekhar K, Yan W, Herrmann D, Sappington A, Bryman GS, et al. Molecular
1231 Classification and Comparative Taxonomics of Foveal and Peripheral Cells in Primate Retina. Cell.
1232 2019;176(5):1222-37 e22. Epub 2019/02/05. doi: 10.1016/j.cell.2019.01.004. PubMed PMID:
1233 30712875; PubMed Central PMCID: PMCPMC6424338.
1234 48. Wool LE, Packer OS, Zaidi Q, Dacey DM. Connectomic Identification and Three-
1235 Dimensional Color Tuning of S-OFF Midget Ganglion Cells in the Primate Retina. J Neurosci.
1236 2019;39(40):7893-909. Epub 2019/08/14. doi: 10.1523/JNEUROSCI.0778-19.2019. PubMed
1237 PMID: 31405926; PubMed Central PMCID: PMCPMC6774400.
1238 49. Rhoades CE, Shah NP, Manookin MB, Brackbill N, Kling A, Goetz G, et al. Unusual
1239 Physiological Properties of Smooth Monostratified Ganglion Cell Types in Primate Retina.
1240 Neuron. 2019;103(4):658-72 e6. Epub 2019/06/23. doi: 10.1016/j.neuron.2019.05.036. PubMed
1241 PMID: 31227309; PubMed Central PMCID: PMCPMC6817368.
1242 50. Dacey DM, Kim YJ, Packer OS, Detwiler PB. ON-OFF direction selective ganglion cells in
1243 macaque monkey retina are tracer-coupled to an ON-OFF direction selective amacrine cell type.
1244 Investigative Ophthalmology & Visual Science. 2019;60(9):5280-.
1245 51. Kim US, Mahroo OA, Mollon JD, Yu-Wai-Man P. Retinal Ganglion Cells—Diversity of Cell
1246 Types and Clinical Relevance. Frontiers in Neurology. 2021;12(635). doi:
1247 10.3389/fneur.2021.661938.
1248 52. Grünert U, Martin PR. Cell types and cell circuits in human and non-human primate
1249 retina. Progress in Retinal and Eye Research. 2020;78:100844. doi:
1250 https://doi.org/10.1016/j.preteyeres.2020.100844.
1251 53. Lee BB, Martin PR, Valberg A. Sensitivity of macaque retinal ganglion cells to chromatic
1252 and luminance flicker. The Journal of physiology. 1989;414:223-43. doi:
1253 10.1113/jphysiol.1989.sp017685. PubMed PMID: 2607430.
1254 54. Lee BB, Pokorny J, Smith VC, Martin PR, Valberg A. Luminance and chromatic
1255 modulation sensitivity of macaque ganglion cells and human observers. J Opt Soc Am A.
1256 1990;7(12):2223-36. Epub 1990/12/01. doi: 10.1364/josaa.7.002223. PubMed PMID: 2090801.
1257 55. Soto F, Hsiang J-C, Rajagopal R, Piggott K, Harocopos GJ, Couch SM, et al. Efficient
1258 Coding by Midget and Parasol Ganglion Cells in the Human Retina. Neuron. 2020;107(4):656-
1259 66.e5. doi: https://doi.org/10.1016/j.neuron.2020.05.030.
1260 56. Brackbill N, Rhoades C, Kling A, Shah NP, Sher A, Litke AM, et al. Reconstruction of
1261 natural images from responses of primate retinal ganglion cells. eLife. 2020;9:e58516. doi:
1262 10.7554/eLife.58516. PubMed PMID: 33146609.
1263 57. Calkins DJ, Schein SJ, Tsukamoto Y, Sterling P. M and L cones in macaque fovea connect
1264 to midget ganglion cells by different numbers of excitatory synapses. Nature.
1265 1994;371(6492):70-2. doi: 10.1038/371070a0.
1266 58. Crook JD, Dacey DM. Circuitry and receptive field structure underlying 'double duty'
1267 performance by midget ganglion cells. Journal of Vision. 2010;10(15):5-. doi: 10.1167/10.15.5.

1268 59. Kaas JH, Guillery RW, Allman JM. Some Principles of Organization in the Dorsal Lateral
1269 Geniculate Nucleus; pp. 253–267. Brain, Behavior and Evolution. 1972;6(1-6):253-67. doi:
1270 10.1159/000123713.
1271 60. Derrington AM, Krauskopf J, Lennie P. Chromatic mechanisms in lateral geniculate
1272 nucleus of macaque. J Physiol. 1984;357:241-65. Epub 1984/12/01. doi:
1273 10.1113/jphysiol.1984.sp015499. PubMed PMID: 6512691; PubMed Central PMCID:
1274 PMCPMC1193257.
1275 61. Solomon SG, Peirce JW, Dhruv NT, Lennie P. Profound contrast adaptation early in the
1276 visual pathway. Neuron. 2004;42(1):155-62. Epub 2004/04/07. doi: 10.1016/s0896-
1277 6273(04)00178-3. PubMed PMID: 15066272.
1278 62. Levitt JB, Schumer RA, Sherman SM, Spear PD, Movshon JA. Visual response properties
1279 of neurons in the LGN of normally reared and visually deprived macaque monkeys. J
1280 Neurophysiol. 2001;85(5):2111-29. Epub 2001/05/16. doi: 10.1152/jn.2001.85.5.2111. PubMed
1281 PMID: 11353027.
1282 63. Gray DC, Merigan W, Wolfing JI, Gee BP, Porter J, Dubra A, et al. In vivo fluorescence
1283 imaging of primate retinal ganglion cells and retinal pigment epithelial cells. Optics express.
1284 2006;14(16):7144-58. Epub 2006/08/07. doi: 10.1364/oe.14.007144. PubMed PMID: 19529085.
1285 64. Yin L, Geng Y, Osakada F, Sharma R, Cetin AH, Callaway EM, et al. Imaging light
1286 responses of retinal ganglion cells in the living mouse eye. J Neurophysiol. 2013;109(9):2415-21.
1287 Epub 2013/02/15. doi: 10.1152/jn.01043.2012. PubMed PMID: 23407356; PubMed Central
1288 PMCID: PMCPMC3652215.
1289 65. Chen T-W, Wardill TJ, Sun Y, Pulver SR, Renninger SL, Baohan A, et al. Ultrasensitive
1290 fluorescent proteins for imaging neuronal activity. Nature. 2013;499(7458):295-300. doi:
1291 10.1038/nature12354. PubMed PMID: 23868258.
1292 66. Yin L, Greenberg K, Hunter JJ, Dalkara D, Kolstad KD, Masella BD, et al. Intravitreal
1293 injection of AAV2 transduces macaque inner retina. Invest Ophthalmol Vis Sci. 2011;52(5):2775-
1294 83. Epub 2011/02/12. doi: 10.1167/iovs.10-6250. PubMed PMID: 21310920; PubMed Central
1295 PMCID: PMCPMC3088562.
1296 67. Chaffiol A, Caplette R, Jaillard C, Brazhnikova E, Desrosiers M, Dubus E, et al. A New
1297 Promoter Allows Optogenetic Vision Restoration with Enhanced Sensitivity in Macaque Retina.
1298 Molecular therapy : the journal of the American Society of Gene Therapy. 2017;25(11):2546-60.
1299 Epub 2017/08/16. doi: 10.1016/j.ymthe.2017.07.011. PubMed PMID: 28807567; PubMed
1300 Central PMCID: PMCPMC5675708.
1301 68. McGregor JE, Godat T, Dhakal K, Parkins K, Strazzeri J, Bateman B, et al. Optogenetic
1302 restoration of retinal ganglion cell activity in the living primate. Nature Communications. 2020.
1303 69. Delori FC, Webb RH, Sliney DH. Maximum permissible exposures for ocular safety (ANSI
1304 2000), with emphasis on ophthalmic devices. J Opt Soc Am A. 2007;24(5):1250-65. doi:
1305 10.1364/JOSAA.24.001250.
1306 70. Schulmeister K. The upcoming new editions of IEC 60825-1 and ANSI Z136.1 – Examples
1307 on impact for classification and exposure limits. International Laser Safety Conference.
1308 2013;2013(1):330-7. doi: 10.2351/1.5056809.
1309 71. Rockwell B, Thomas R, Zimmerman S. Updates to the ANSI Z136.1 standard.
1310 International Laser Safety Conference. 2015;2015(1):75-7. doi: 10.2351/1.5056858.
1311 72. Geng Y, Dubra A, Yin L, Merigan WH, Sharma R, Libby RT, et al. Adaptive optics retinal
1312 imaging in the living mouse eye. Biomedical optics express. 2012;3(4):715-34. Epub 2012/05/11.
1313 doi: 10.1364/boe.3.000715. PubMed PMID: 22574260; PubMed Central PMCID:
1314 PMCPMC3345801.

73. Atchison DA, Smith G. Chromatic dispersions of the ocular media of human eyes. J Opt Soc Am A. 2005;22(1):29-37. doi: 10.1364/JOSAA.22.000029.
74. Nelder JA, Mead R. A Simplex Method for Function Minimization. The Computer Journal. 1965;7(4):308-13. doi: 10.1093/comjnl/7.4.308.
75. Rossi EA, Granger CE, Sharma R, Yang Q, Saito K, Schwarz C, et al. Imaging individual neurons in the retinal ganglion cell layer of the living eye. Proceedings of the National Academy of Sciences of the United States of America. 2017;114(3):586-91. Epub 2017/01/05. doi: 10.1073/pnas.1613445114. PubMed PMID: 28049835; PubMed Central PMCID: PMCPMC5255596.
76. Baron WS. Maxwellian view stimulator for electrophysiological or psychophysical work. Applied optics. 1973;12(11):2560-2. Epub 1973/11/01. doi: 10.1364/AO.12.002560. PubMed PMID: 20125830.
77. Schnapf JL, Kraft TW, Nunn BJ, Baylor DA. Spectral sensitivity of primate photoreceptors. Vis Neurosci. 1988;1(3):255-61. Epub 1988/01/01. PubMed PMID: 3154798.
78. Snodderly DM, Auran JD, Delori FC. The macular pigment. II. Spatial distribution in primate retinas. Invest Ophthalmol Vis Sci. 1984;25(6):674-85. Epub 1984/06/01. PubMed PMID: 6724837.
79. Snodderly DM, Brown PK, Delori FC, Auran JD. The macular pigment. I. Absorbance spectra, localization, and discrimination from other yellow pigments in primate retinas. Invest Ophthalmol Vis Sci. 1984;25(6):660-73. Epub 1984/06/01. PubMed PMID: 6724836.
80. Lamb TD. Photoreceptor spectral sensitivities: Common shape in the long-wavelength region. Vision Research. 1995;35(22):3083-91. doi: https://doi.org/10.1016/0042-6989(95)00114-F.
81. Govardovskii VI, Fyhrquist N, Reuter TOM, Kuzmin DG, Donner K. In search of the visual pigment template. Visual Neuroscience. 2000;17(4):509-28. Epub 2000/07/01. doi: 10.1017/S0952523800174036.
82. Bowmaker JK. Cone Visual Pigments in Monkeys and Humans. Advances in Photoreception: Proceedings of a Symposium on Frontiers of Visual Science: National Academies Press; 1990.
83. Boettner EA. Spectral Transmission of the Eye. The University of Michigan, Final Report, Air Force Contract F41(609)-2966. 1967.
84. Dobkins KR, Thiele A, Albright TD. Comparison of red-green equiluminance points in humans and macaques: evidence for different L:M cone ratios between species. Journal of the Optical Society of America A, Optics, image science, and vision. 2000;17(3):545-56. Epub 2000/03/09. PubMed PMID: 10708036.
85. Estevez O, Spekreijse H. The "silent substitution" method in visual research. Vision Res. 1982;22(6):681-91. Epub 1982/01/01. doi: 10.1016/0042-6989(82)90104-3. PubMed PMID: 7112962.
86. Brainard DH. The Psychophysics Toolbox. Spat Vis. 1997;10(4):433-6. Epub 1997/01/01. PubMed PMID: 9176952.
87. Passaglia CL, Troy JB, Rüttiger L, Lee BB. Orientation sensitivity of ganglion cells in primate retina. Vision Research. 2002;42(6):683-94. doi: https://doi.org/10.1016/S0042-6989(01)00312-1.
88. Yang Q, Zhang J, Nozato K, Saito K, Williams DR, Roorda A, et al. Closed-loop optical stabilization and digital image registration in adaptive optics scanning light ophthalmoscopy. Biomedical optics express. 2014;5(9):3174-91. Epub 2014/11/18. doi: 10.1364/boe.5.003174. PubMed PMID: 25401030; PubMed Central PMCID: PMCPMC4230869.

1362 89. Ku HH. Notes on the use of propagation of error formulas. Journal of Research of the
1363 National Bureau of Standards. 1966;70(4):263-73.
1364 90. Enroth-Cugell C, Robson JG. The contrast sensitivity of retinal ganglion cells of the cat. J
1365 Physiol. 1966;187(3):517-52. Epub 1966/12/01. doi: 10.1113/jphysiol.1966.sp008107. PubMed
1366 PMID: 16783910; PubMed Central PMCID: PMCPMC1395960.
1367 91. Cottaris NP, Jiang H, Ding X, Wandell BA, Brainard DH. A computational-observer model
1368 of spatial contrast sensitivity: Effects of wave-front-based optics, cone-mosaic structure, and
1369 inference engine. Journal of Vision. 2019;19(4):8-. doi: 10.1167/19.4.8.
1370 92. Cottaris NP, Wandell BA, Rieke F, Brainard DH. A computational observer model of
1371 spatial contrast sensitivity: Effects of photocurrent encoding, fixational eye movements, and
1372 inference engine. Journal of Vision. 2020;20(7):17-. doi: 10.1167/jov.20.7.17.
1373 93. Stockman A, Sharpe LT, Fach C. The spectral sensitivity of the human short-wavelength
1374 sensitive cones derived from thresholds and color matches. Vision Res. 1999;39(17):2901-27.
1375 Epub 1999/09/24. doi: 10.1016/s0042-6989(98)00225-9. PubMed PMID: 10492818.
1376 94. Stockman A, Sharpe LT. The spectral sensitivities of the middle- and long-wavelength-
1377 sensitive cones derived from measurements in observers of known genotype. Vision Research.
1378 2000;40(13):1711-37. doi: https://doi.org/10.1016/S0042-6989(00)00021-3.
1379 95. Pokorny J, Smith VC, Lutze M. Aging of the human lens. Applied optics. 1987;26(8):1437-
1380 40. doi: 10.1364/AO.26.001437.
1381 96. Dalkara D, Kolstad KD, Caporale N, Visel M, Klimczak RR, Schaffer DV, et al. Inner limiting
1382 membrane barriers to AAV-mediated retinal transduction from the vitreous. Molecular therapy :
1383 the journal of the American Society of Gene Therapy. 2009;17(12):2096-102. Epub 2009/08/13.
1384 doi: 10.1038/mt.2009.181. PubMed PMID: 19672248; PubMed Central PMCID:
1385 PMCPMC2814392.
1386 97. Helga Kolb EF, Ralph N. Webvision : the organization of the retina and visual system:
1387 [Bethesda, Md.] : National Library of Medicine : [National Center for Biotechnology
1388 Information], 2007.; 2007.
1389 98. Yan W, Peng Y-R, van Zyl T, Regev A, Shekhar K, Juric D, et al. Cell Atlas of The Human
1390 Fovea and Peripheral Retina. Scientific reports. 2020;10(1):9802. doi: 10.1038/s41598-020-
1391 66092-9.
1392 99. Packer O, Hendrickson AE, Curcio CA. Photoreceptor topography of the retina in the
1393 adult pigtail macaque (Macaca nemestrina). Journal of Comparative Neurology.
1394 1989;288(1):165-83. doi: https://doi.org/10.1002/cne.902880113.
1395 100. Jaeken B, Artal P. Optical quality of emmetropic and myopic eyes in the periphery
1396 measured with high-angular resolution. Investigative Ophthalmology & Visual Science.
1397 2012;53(7):3405-13.
1398 101. Provis JM, Hendrickson AE. The Foveal Avascular Region of Developing Human Retina.
1399 Archives of Ophthalmology. 2008;126(4):507-11. doi: 10.1001/archopht.126.4.507.
1400 102. Croner LJ, Purpura K, Kaplan E. Response variability in retinal ganglion cells of primates.
1401 Proceedings of the National Academy of Sciences. 1993;90(17):8128-30. doi:
1402 10.1073/pnas.90.17.8128.
1403 103. Greschner M, Shlens J, Bakolitsa C, Field GD, Gauthier JL, Jepson LH, et al. Correlated
1404 firing among major ganglion cell types in primate retina. J Physiol. 2011;589(Pt 1):75-86. Epub
1405 2010/10/06. doi: 10.1113/jphysiol.2010.193888. PubMed PMID: 20921200; PubMed Central
1406 PMCID: PMCPMC3039261.
1407 104. Greschner M, Field GD, Li PH, Schiff ML, Gauthier JL, Ahn D, et al. A polyaxonal amacrine
1408 cell population in the primate retina. J Neurosci. 2014;34(10):3597-606. Epub 2014/03/07. doi:

1409 10.1523/JNEUROSCI.3359-13.2014. PubMed PMID: 24599459; PubMed Central PMCID:
1410 PMCPMC3942577.
1411 105. Fan VH, Grosberg LE, Madugula SS, Hottowy P, Dabrowski W, Sher A, et al. Epiretinal
1412 stimulation with local returns enhances selectivity at cellular resolution. Journal of neural
1413 engineering. 2019;16(2):025001. Epub 2018/12/14. doi: 10.1088/1741-2552/aaeef1. PubMed
1414 PMID: 30523958; PubMed Central PMCID: PMCPMC6416068.
1415 106. Miller DT, Kurokawa K. Cellular-Scale Imaging of Transparent Retinal Structures and
1416 Processes Using Adaptive Optics Optical Coherence Tomography. Annual review of vision
1417 science. 2020;6(1):115-48. doi: 10.1146/annurev-vision-030320-041255. PubMed PMID:
1418 32609578.
1419 107. Soltanian-Zadeh S, Kurokawa K, Liu Z, Zhang F, Saeedi O, Hammer DX, et al. Weakly
1420 supervised individual ganglion cell segmentation from adaptiveoptics OCT images for
1421 glaucomatous damage assessment. Optica. 2021;8(5):642-51. doi: 10.1364/OPTICA.418274.
1422 108. Hampson KM, Turcotte R, Miller DT, Kurokawa K, Males JR, Ji N, et al. Adaptive optics for
1423 high-resolution imaging. Nature Reviews Methods Primers. 2021;1(1):68. doi: 10.1038/s43586-
1424 021-00066-7.
1425 109. Bumsted K, Hendrickson A. Distribution and development of short-wavelength cones
1426 differ between Macaca monkey and human fovea. J Comp Neurol. 1999;403(4):502-16. Epub
1427 1999/01/15. PubMed PMID: 9888315.
1428 110. Patterson SS, Neitz M, Neitz J. Reconciling Color Vision Models With Midget Ganglion
1429 Cell Receptive Fields. Front Neurosci. 2019;13:865. Epub 2019/09/03. doi:
1430 10.3389/fnins.2019.00865. PubMed PMID: 31474825; PubMed Central PMCID:
1431 PMCPMC6707431.
1432 111. Tailby C, Solomon SG, Lennie P. Functional Asymmetries in Visual Pathways Carrying S-
1433 Cone Signals in Macaque. The Journal of Neuroscience. 2008;28(15):4078-87. doi:
1434 10.1523/jneurosci.5338-07.2008.
1435 112. van der Schaaf A, van Hateren JH. Modelling the Power Spectra of Natural Images:
1436 Statistics and Information. Vision Research. 1996;36(17):2759-70. doi:
1437 https://doi.org/10.1016/0042-6989(96)00002-8.
1438 113. Lee BB, Sun H. The chromatic input to cells of the magnocellular pathway of primates.
1439 Journal of vision. 2009;9(2):1-18. doi: 10.1167/9.2.15. PubMed PMID: 19271925.
1440 114. Diller L, Packer OS, Verweij J, McMahon MJ, Williams DR, Dacey DM. L and M cone
1441 contributions to the midget and parasol ganglion cell receptive fields of macaque monkey
1442 retina. J Neurosci. 2004;24(5):1079-88. Epub 2004/02/06. doi: 10.1523/JNEUROSCI.3828-
1443 03.2004. PubMed PMID: 14762126; PubMed Central PMCID: PMCPMC6793593.

1444

1445

1446 # Supporting information

1447 **S1 Fig. AOSLO System Diagram.** The adaptive optics scanning light ophthalmoscope used in this
1448 study consists of three main arms or subsystems. First, the Source arm, contains the 488 nm laser
1449 used to excite GCaMP fluorescence, the 561 nm laser used as visual stimulation as in the drifting
1450 gratings, the 796 superluminescent diode used to image the cone photoreceptors, and the 843
1451 nm laser diode used for wavefront sensing and correction. Each source is co-aligned and
1452 combined with dichroic mirrors so that at the output of the arm they exit coaxial with each other
1453 along the same beam path into the system. 90% of the source power is lost at a 90/10
1454 beamsplitter such that 10% of the source power enters the Sample arm of the system—this is
1455 done so that on the back-pass, 90% of the signal is transmitted to the detectors while only 10% of
1456 the signal is lost. The Sample arm is composed of various optical telescopes (whose function is to
1457 translate the beam axially and change the magnification to match the pupil sizes of the various
1458 active elements) and four important planes conjugate to the pupil. The first two conjugate planes
1459 are the vertical (VS) and horizontal (HS) scanners which raster scan the beam across a rectangular
1460 field of view. The third conjugate plane is the deformable mirror (DM) which changes shape to
1461 correct the measured wavefront aberrations of the animal's eye to provide near-diffraction
1462 limited imaging of the retina. The fourth conjugate plane is the pupil of the animal's eye, where
1463 all source light enters and from which all detected light emanates. In the Detection arm, two
1464 photomultiplier tubes (PMT) detect visible fluorescence (VIS) from the emitted GCaMP signal and
1465 infrared (REF) reflected light from the cone photoreceptors. A Shack-Hartmann wavefront sensor
1466 (SHWS) collectes infrared light from the 843 nm source and measures the wavefront aberrations
1467 of the animal's eye, sending that information to the deformable mirror in a closed loop. Finally, a
1468 Maxwellian View subsystem is used to inject the LED stimulation lights into the system near the

1469 pupil plane (bypassing both scanners and the deformable mirror). The subsystem contains LEDs
1470 at 420 nm, 470 nm, 530 nm, and 660 nm, although the 470 nm LED was not used in this study.
1471 Just as in the Source arm, the LEDs are co-aligned and combined using dichroic mirrors so they
1472 follow the same beam path. The LEDs pass through a spatial filter which removes any spatial
1473 inhomogeneities and then through a field stop which restricts the beam sizes on the retina to a
1474 circular subsection of the fovea about 1.3 degrees in diameter. The LEDs are reflected into the
1475 system via a pellicle beamsplitter which has 88% transmission (throws away 88% of the LED source
1476 power, but allows 88% of the signal to pass on the way to the detectors).

1477 **S2 Fig. Examples of raw fluorescence time courses of putative midget cells to various stimuli.**
1478 Six of the putative midget cells identified from the foveola of animal M3 are shown in detail. For
1479 each cell, the fluorescence time course is shown for that cell for six different stimuli: the L-isolating
1480 0.15 Hz flicker, the M-isolating 0.15 Hz flicker, the S-isolating 0.15 Hz flicker, the 9.2 cyc/deg 6 Hz
1481 drifting grating, the 28.3 cyc/deg 6 Hz drifting grating, and the 49.1 cyc/deg 6 Hz drifting grating.
1482 For each stimulus, there are three fluorescence traces corresponding to experiment one (blue),
1483 experiment two (orange), and experiment three (yellow), which all occurred approximately a
1484 week apart. There is a fourth fluorescence trace (black) that is the average over the three
1485 experiments shown. Each fluorescence time course was normalized to the peak response for that
1486 cell, and a moving window (MATLAB movmean()) was used to smooth each fluorescence time
1487 course with a width of three seconds for the L/M/S isolating stimuli and a width of 5 seconds for
1488 the drifting grating stimuli. Note that as described in the manuscript, the L and M isolating stimuli
1489 are characterized by a modulation of the fluorescence near the stimulus frequency of 0.15 Hz. As
1490 these six cells were all putative midgets, note that the S isolating responses do not have the same
1491 modulation frequency, and are mainly affected by the respiration rate of the animal which causes

small residual motion of the eye (approximately 0.28 Hz in M3). Note that as described in the manuscript, the drifting grating responses are characterized by a sustained increase in the mean fluorescence as opposed to a modulation, since the drifting speed exceeded the GCaMP6 temporal sensitivity.

S3 Fig. Variability of responses to chromatic and achromatic flicker. Plots for the small FOV from M3 show the response variability to the L isolating, M isolating, S isolating, and Luminance stimuli. Note that these are boxplots showing the median, 25-75% interquartile range, and lowest and highest values, but there were only three measurements. Thus, the median value and the two ends of the boxplots represent the three measured values for each cell. For the large FOV from M3 and M2, there are many more cells, so the standard error divided by the mean SNR is plotted as a histogram for all cells that were responsive to each individual stimulus. No standard error can be plotted for M1, as there was only one experiment in that animal.

S4 Fig. Soma sizes of RGCs for animals M2 and M3 across chromatic functional groups. Observer 1 used the open source software GIMP to segment RGCs in fluorescence images from M2 (large FOV), M3 (large FOV) and M3 (small FOV). The ellipse tool was used to segment the rough boundary of individual RGCs. Observer 2 used the open source software ImageJ to segment the same RGCs in fluorescence images from M2 and M3 using a hand tracing tool to trace the observable edges of each cell's fluorescence. Under both methods, the area for each cell was computed in terms of pixels^2 and then converted to µm^2 using the following formula: $\frac{\mu m}{pixel} = 291.2\ \frac{\mu m}{deg} * \frac{axial\ length}{24.2\ mm} * \frac{FOV\ width}{496\ pixels}$, where 291.2 µm/deg is the human model eye visual angle to retinal extent conversion, 24.2 mm is the human model eye axial length, 496 pixels is the width of the imaging PMT used in the AOSLO system, axial length is the animal's axial length in mm, and

1515 FOV width is the width in degrees of the FOV used. The axial length of animal M2 is 17.2 mm, and
1516 the FOV width used was 3.64 deg. The axial length of animal M3 is 16.56 mm, and the FOV widths
1517 used were 3.69 deg (large FOV) and 2.54 deg (small FOV). Cells were compared across functional
1518 groups identified as L-M/M-L chromatic opponent (L-M), S only responding (S), Luminance only
1519 or achromatic (LUM), and mixed L-M/S responses (L-M/S). In **(a)**, the soma areas in μm^2 for the
1520 four functional groups in M2 are listed as the mean and standard deviation of each group across
1521 both observers. In **(b)**, the same comparisons are made for the four functional groups in M3 at
1522 the large FOV. In **(c)**, comparisons for the two functional groups found in M3 at the inner edge of
1523 the foveal slope (small FOV) are made across both observers. In, **(d)**, summary tables show the p-
1524 scores from a Mann-Whitney U test (MATLAB function ranksum(x,y)) comparing the distributions
1525 of soma areas across functional groups as measured by both observers separately. All p-values
1526 were greater than 0.1, except for Observer 2's comparison of the L-M group to the S only group
1527 in M2 which had p = 0.0118. Based on these results, we cannot reject the hypothesis that the
1528 distributions of soma sizes for these functional groups are roughly the same across the two
1529 animals measured at the range of eccentricities at which we imaged cell somas.
1530
1531 **S5 Fig. Spatial response of RGCs from M3 in the large FOV condition.** Some example responses
1532 of L-M/M-L chromatic opponent RGCs from M3 at the large FOV, where each plot is the response
1533 of a different cell to drifting gratings (6 Hz) of spatial frequencies from 2 – 34 c/deg. These cells
1534 were chosen to showcase different cell responses and are not necessarily special or
1535 representative of the population. Purple and Orange curves show two separate experiments that
1536 were averaged together (Gray curve). The Blue curves are simple difference of Gaussians fits (not
1537 the full ISETBio modeling, for reasons explained below) to each average. Each plot title includes
1538 the cell's unique label "cN", and five parameters—the center strength K_c, the center radius r_c, the

1539 surround strength K_s, the surround radius r_s, and a goodness of fit value for the difference of
1540 Gaussians. As can be easily seen, many of the cells do not exhibit high spatial frequency falloff at
1541 the range of spatial frequencies measured, and so the difference of Gaussians either fits poorly
1542 or produces fit parameters that are highly irregular or suspect such as center sizes much smaller
1543 than the size of a single cone. For this reason, these data were not incorporated into the modelling
1544 in the main body, as higher spatial frequency responses were needed to properly fit many of these
1545 cell responses. There were 48 such L-M/M-L chromatic opponent cells in the large FOV in M3 out
1546 of 145 measured cells. In M2, there was only one experiment measuring response to spatial
1547 frequency and it suffered from the same lack of high spatial frequency measurements as the data
1548 shown here. Full data from both animals can be shared upon request.
1549
1550 **S6 Fig. Spatial response of achromatic RGCs from M3 at the center of the foveola.** Each graph
1551 represents a single cell identified as responding only to achromatic stimuli from the center of the
1552 foveola of M3. The measured responses were to drifting gratings (6 Hz) of spatial frequencies
1553 from 4 – 49 c/deg. Purple, Orange, and Green lines represent the cell's response in three different
1554 experiments. The Gray line is the average of the three experiments for each cell, and the Blue line
1555 is a simple difference of Gaussians fit to the average (not the full ISETBio model, see S5 Fig). Each
1556 plot title includes the cell's unique label "cN", and five parameters—the center strength K_c, the
1557 center radius r_c, the surround strength K_s, the surround radius r_s, and a goodness of fit value for
1558 the difference of Gaussians. Compared to the 15 L-M and M-L cone opponent cells from this same
1559 location, these 7 achromatic cells were had noisier responses across experiments and more varied
1560 response characteristics. Though most of these cells are likely to be parasol RGCs, some could be
1561 achromatic midget RGCs or other rarer achromatic RGC types. Due to this uncertainty, these data
1562 were not included in the modelling for putative midget RGCs presented in the main manuscript.

There were also achromatic cells identified in M2 and in M3 at the large FOV condition, but those data suffer from decreased resolution and a decreased range of spatial frequencies presented to the cells. Full data from all animals can be shared upon request.

S7 Fig. Cone mosaic modelling fits compared to data from M3. Images showing the performance of the ISETBio cone mosaic generator compared to the actual data from M3. At top, the model trichromatic photoreceptor mosaic generated by ISETBio (left) and the corresponding model cone density (right) (compare to Fig. 1b). At bottom left, a comparison of the median diameter of cones are compared between the model and the M3 data. At bottom middle and bottom right, the cone diameters of the model and measured data from M3 are compared across the horizontal and vertical meridians respectively.

S8 Fig. Model cross-validation. RMS errors for the 4 modeling scenarios we considered are depicted for 12 cells. Yellow and blue bars indicate insample and out-of-sample performance, respectively. During in-sample performance assessment the model is trained and evaluated using data from the same recording session. During out-of-sample performance assessment, the model is trained in one session and evaluated using data from another session. The data do not have enough power to reveal a model with best generalizing (out-of-sample) performance. In a few cells, the 1-cone/0.00D residual defocus model can be ruled out as its performance is significantly worse than the remaining 3. A two sample t-test with unequal variance was used to test against the hypothesis that there is a significant difference in the mean RMS fit errors between 2 modeling scenarios.

1586 **S9 Fig. Optimization of residual defocus for different RGCs.** For each cell the optimal residual
1587 defocus value for the single cone center and multi-cone center model scenarios was calculated to
1588 gauge variability from the chosen 0.067 D reported in the main text. For each cell, the RMSE is
1589 shown for various residual defocus values for both model scarios. Cells are labeled L1-11 or M1-4
1590 according to whether we believed they were likely to contain an L cone or M cone at their center.
1591
1592 **S10 Fig. All four model scenario fits for the 15 L-M and M-L cone opponent RGCs from the center**
1593 **of the fovea of M3.** Four model scenarios were considered for all 15 cells: single cone centers
1594 with 0 D residual defocus, single cone centers with 0.067 D residual defocus, multi-cone centers
1595 with 0 D residual defocus, and multi-cone centers with 0.067 D residual defocus. As can be seen
1596 from the fits, the single cone center with 0.067 D defocus performs well for all 15 cells and
1597 produces center-surround structures that are consistent with what has been measured from
1598 physiology. Cells are labeled L1-11 or M1-4 according to whether we believed they were likely to
1599 contain an L cone or M cone at their center.
1600
1601 **S11 Fig. Simple center-surround model estimating percentage of achromatic midget RGCs.** A
1602 simple model cone mosaic using hexagonal packing was created in MATLAB for the centermost
1603 2400 cones (radius of 25 cones from the foveal center). Each cone was randomly assigned to be
1604 an L cone (48%), M cone (48%), or S cone (4%). For this simple model, a midget RGC was assumed
1605 to connect to one cone at its receptive field center and 6 cones at its surround (immediately
1606 adjacent to the center cone). For each model midget RGC, the proportion of cones that were the
1607 same type as the center cone was calculated. RGCs with all 6 surround cones of the same type as
1608 the center were classified as 'true achromatic' (orange histogram), and RGCs with at least 5
1609 surround cones of the same type as the center were classified as 'thresholded achromatic' (blue

histogram). The entire model simulation was then repeated 10,000 times, with a different randomly assigned cone mosaic each time. The histograms above show the number of simulations for which each percentage of midget RGCs that were either true achromatic or thresholded achromatic occurred. Based on this simple model, truly achromatic midget RGCs might make up approximately 1.5% of total midget RGCs at the foveal center, while thresholded achromatic midget RGCs might make up approximately 9% of total midget RGCs at the foveal center.

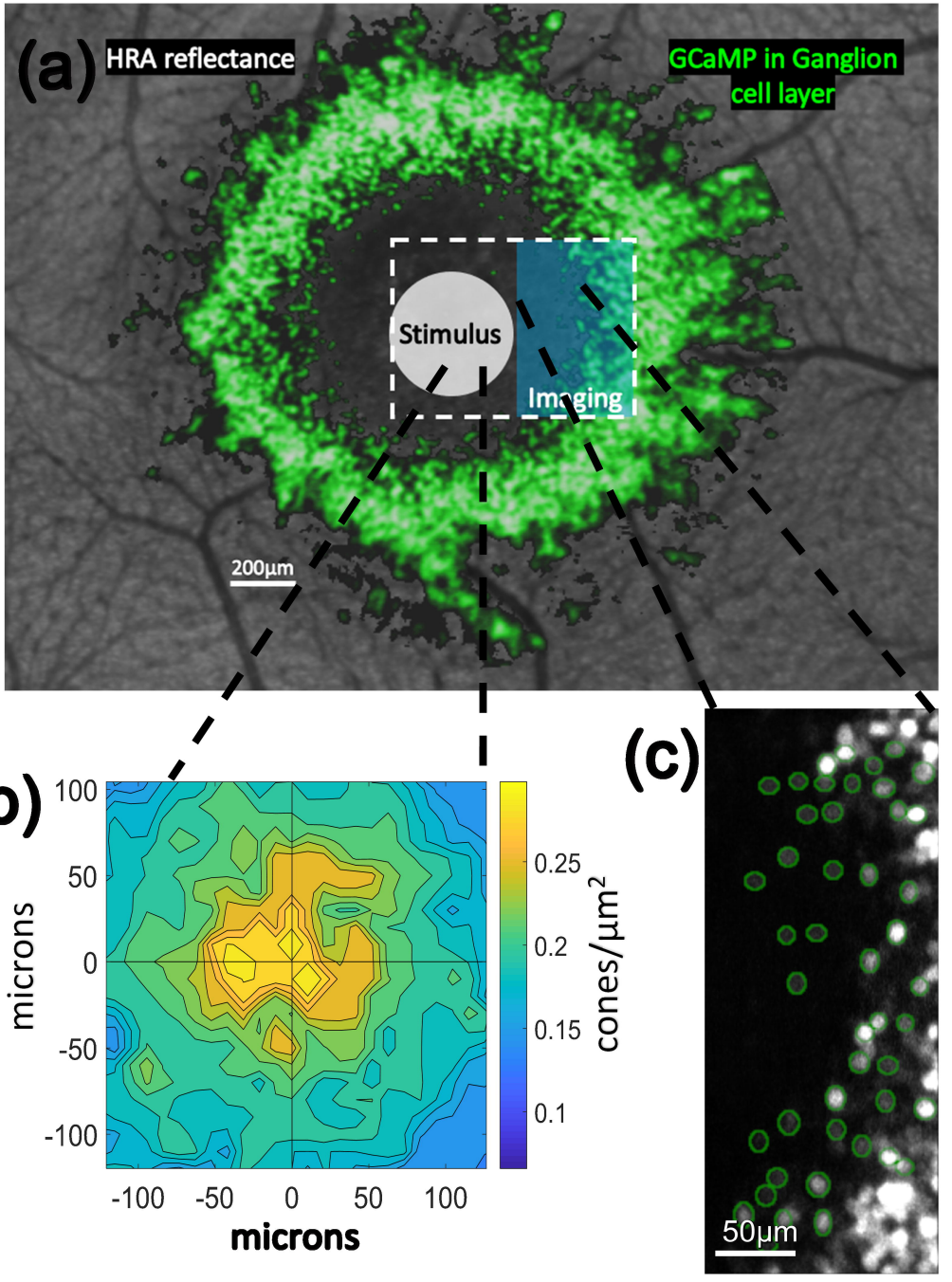
(a)
HRA reflectance
GCaMP in Ganglion cell layer
Stimulus
Imaging
200µm
(b)
100
50
0
-50
-100
microns
-100
-50
0
50
100
microns
0.25
0.2
0.15
0.1
cones/µm²
(c)
50µm

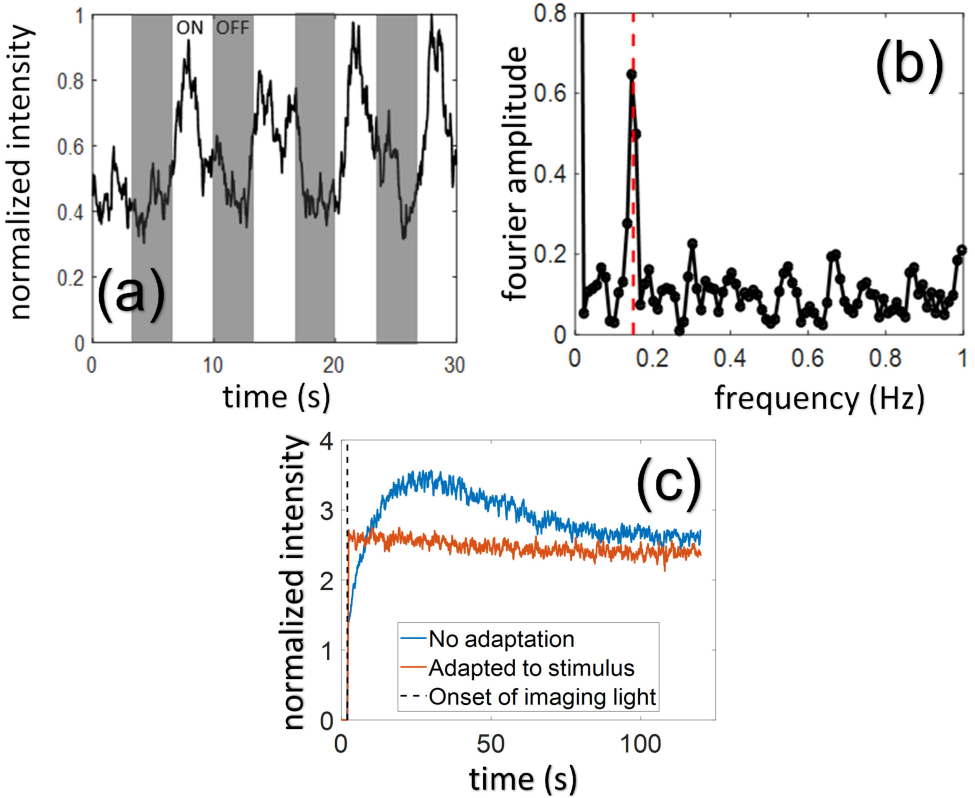
(a)
ON
OFF
normalized intensity
time (s)
(b)
fourier amplitude
frequency (Hz)
(c)
normalized intensity
time (s)
No adaptation
Adapted to stimulus
Onset of imaging light

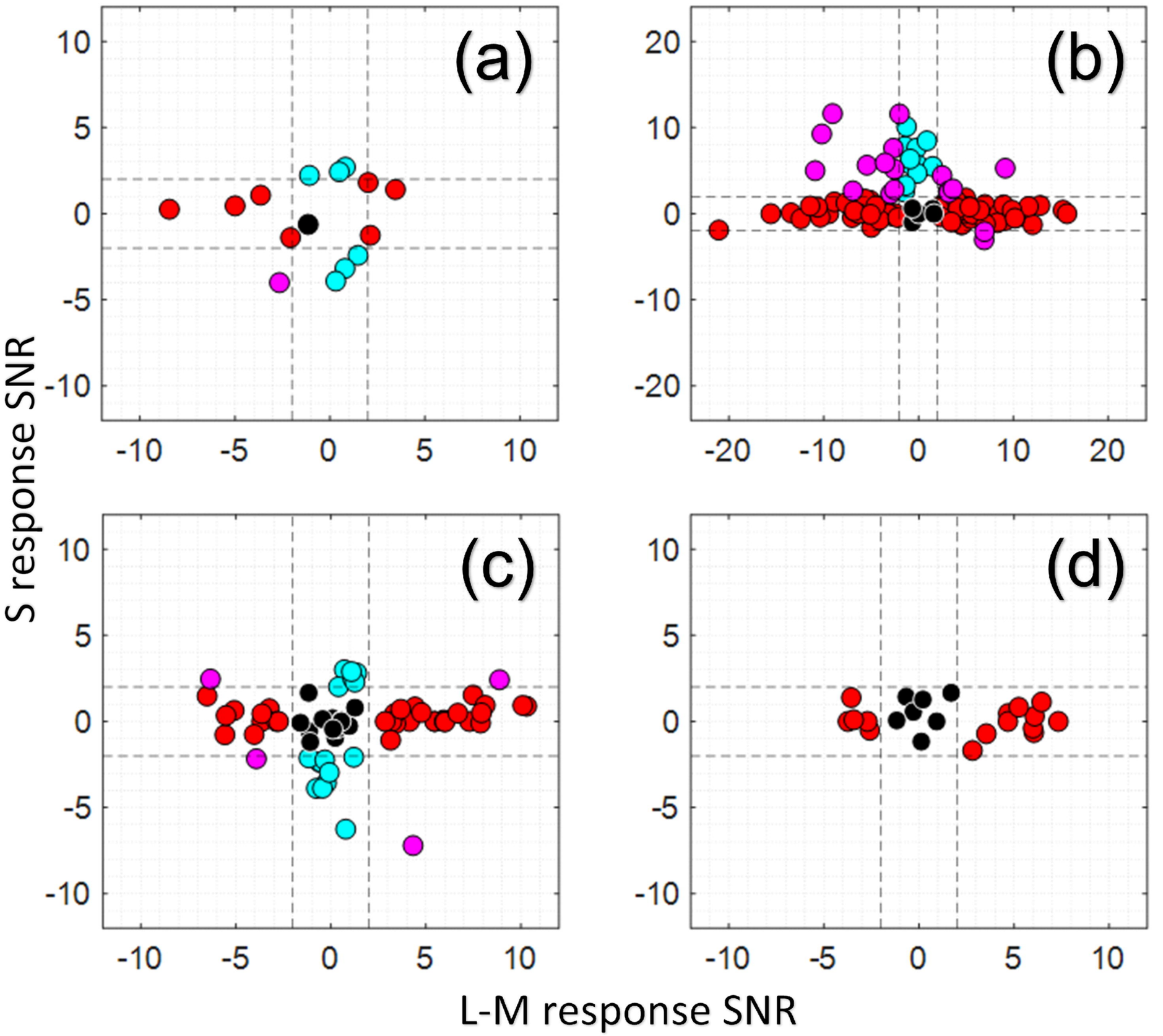
(a)
(b)
(c)
(d)
S response SNR
L-M response SNR
10
5
0
-5
-10
20
10
0
-10
-20
-10
-5
0
5
10
-20
-10
0
10
20

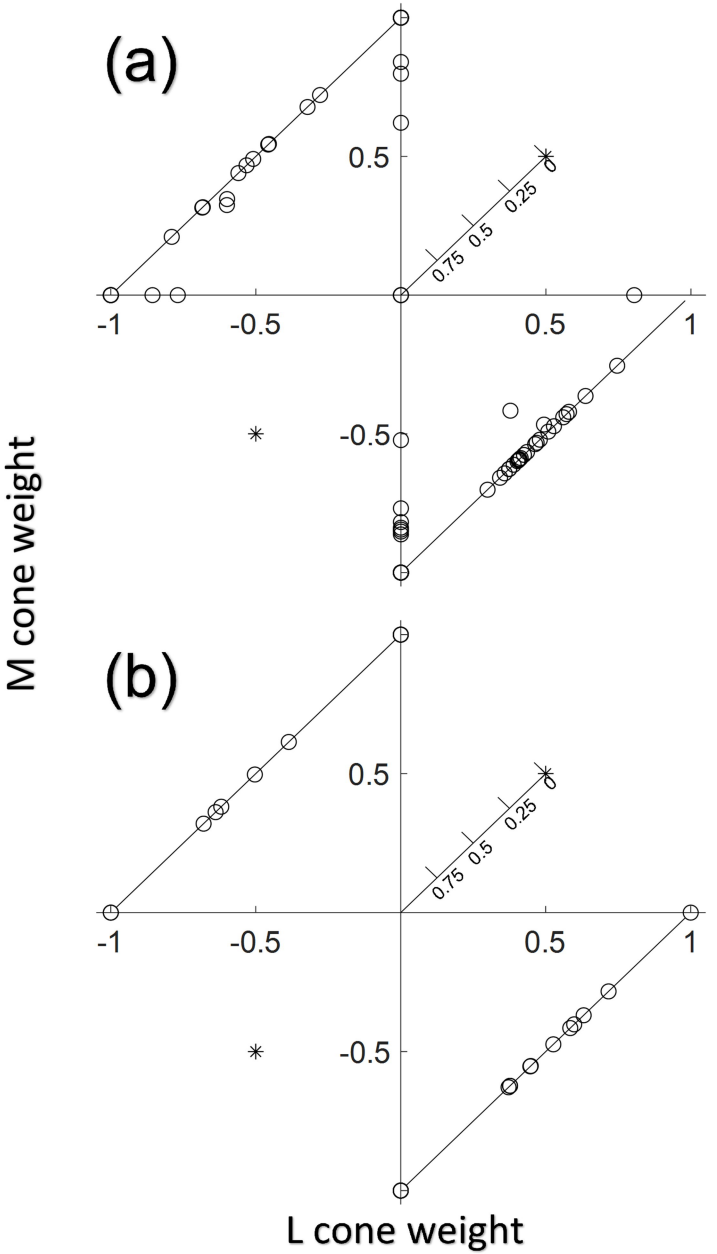
(a)
0.5
-0.5
-1
-0.5
0.5
1
0
0.25
0.5
0.75
(b)
0.5
-0.5
-1
-0.5
0.5
1
0
0.25
0.5
0.75
M cone weight
L cone weight

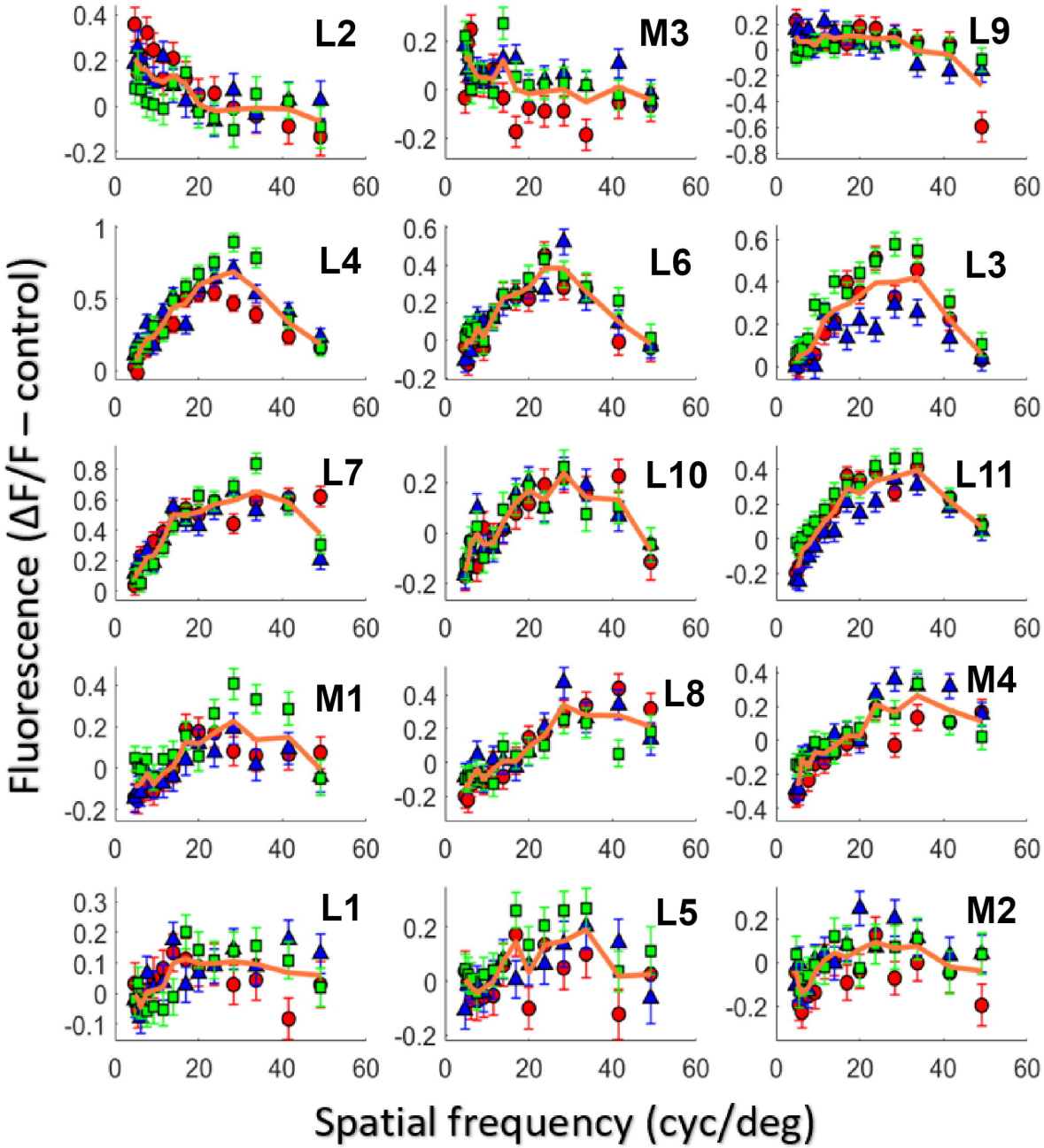
L2
M3
L9
L4
L6
L3
L7
L10
L11
M1
L8
M4
L1
L5
M2
Fluorescence (ΔF/F – control)
Spatial frequency (cyc/deg)

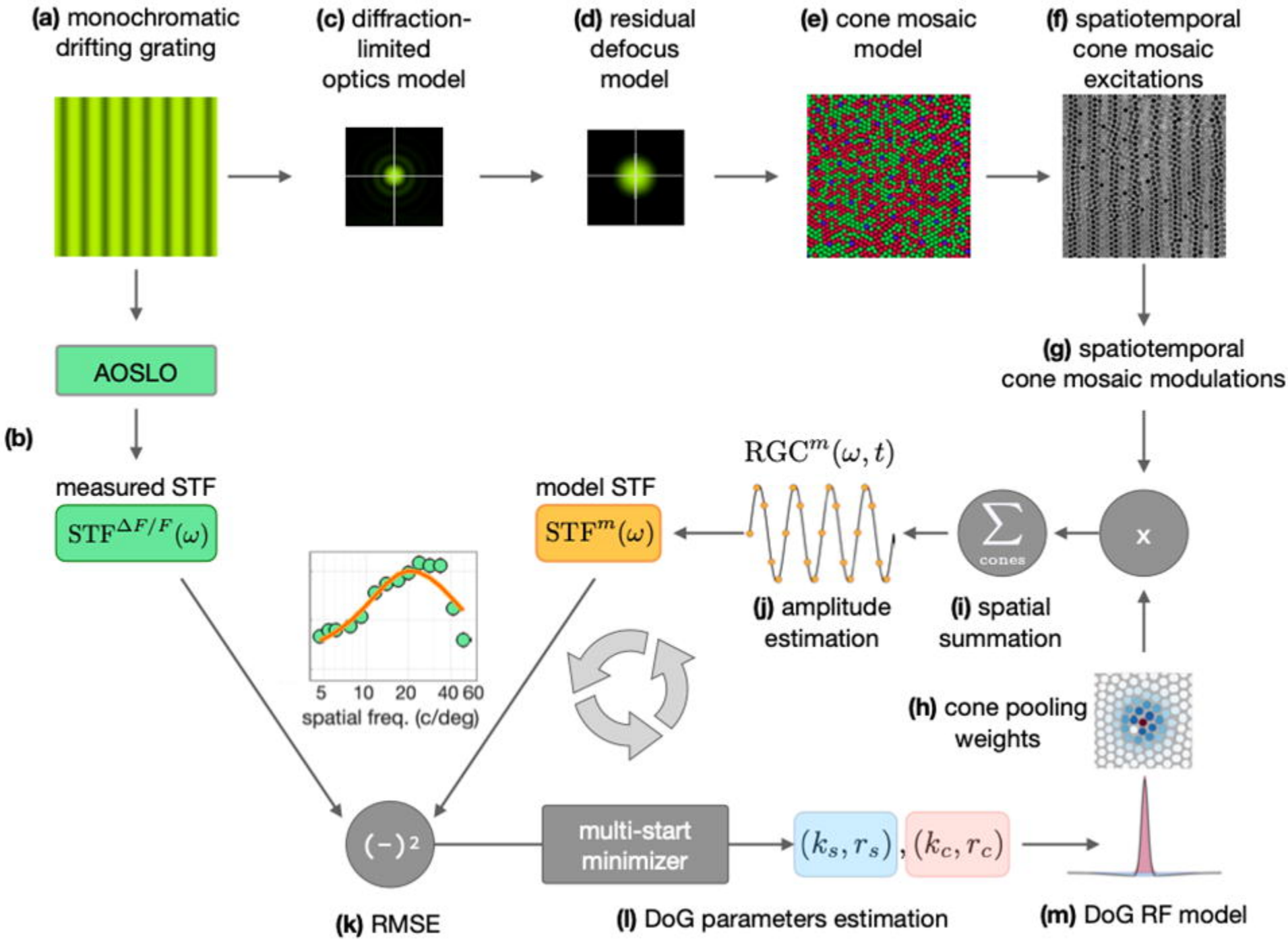
(a) monochromatic drifting grating
(c) diffraction-limited optics model
(d) residual defocus model
(e) cone mosaic model
(f) spatiotemporal cone mosaic excitations
AOSLO
(b)
measured STF
$\mathrm{STF}^{\Delta F/F}(\omega)$
model STF
$\mathrm{STF}^{m}(\omega)$
$\mathrm{RGC}^{m}(\omega, t)$
(g) spatiotemporal cone mosaic modulations
x
cones
(i) spatial summation
(j) amplitude estimation
5 10 20 40 60
spatial freq. (c/deg)
(h) cone pooling weights
$(-)^2$
multi-start minimizer
$(k_s, r_s), (k_c, r_c)$
(k) RMSE
(l) DoG parameters estimation
(m) DoG RF model

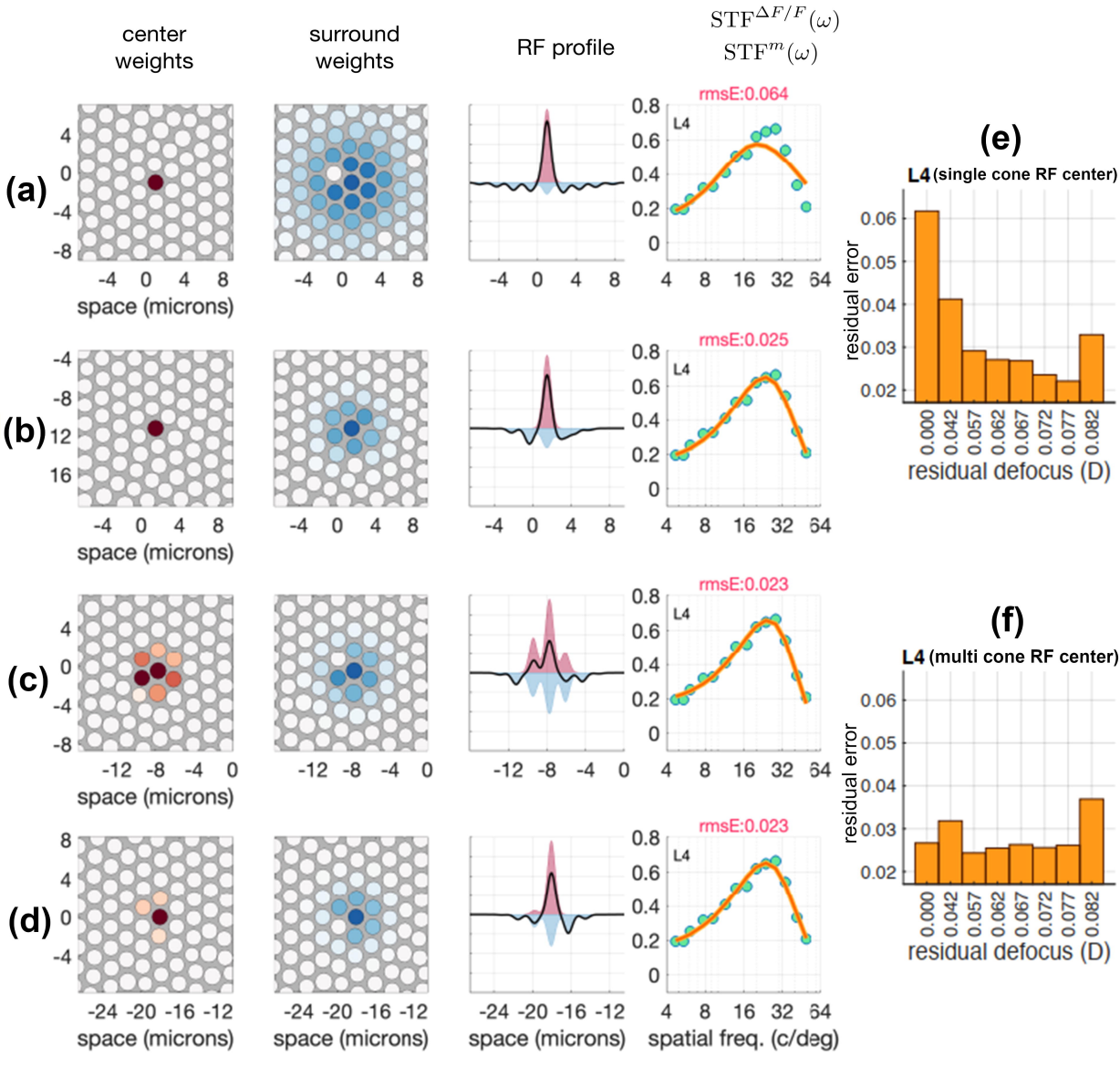
center weights
surround weights
RF profile
$\mathrm{STF}^{\Delta F/F}(\omega)$
$\mathrm{STF}^{m}(\omega)$
(a)
(b)
(c)
(d)
rmsE:0.064
rmsE:0.025
rmsE:0.023
rmsE:0.023
L4
space (microns)
spatial freq. (c/deg)
(e)
L4 (single cone RF center)
(f)
L4 (multi cone RF center)
residual error
residual defocus (D)
0.000
0.042
0.057
0.062
0.067
0.072
0.077
0.082

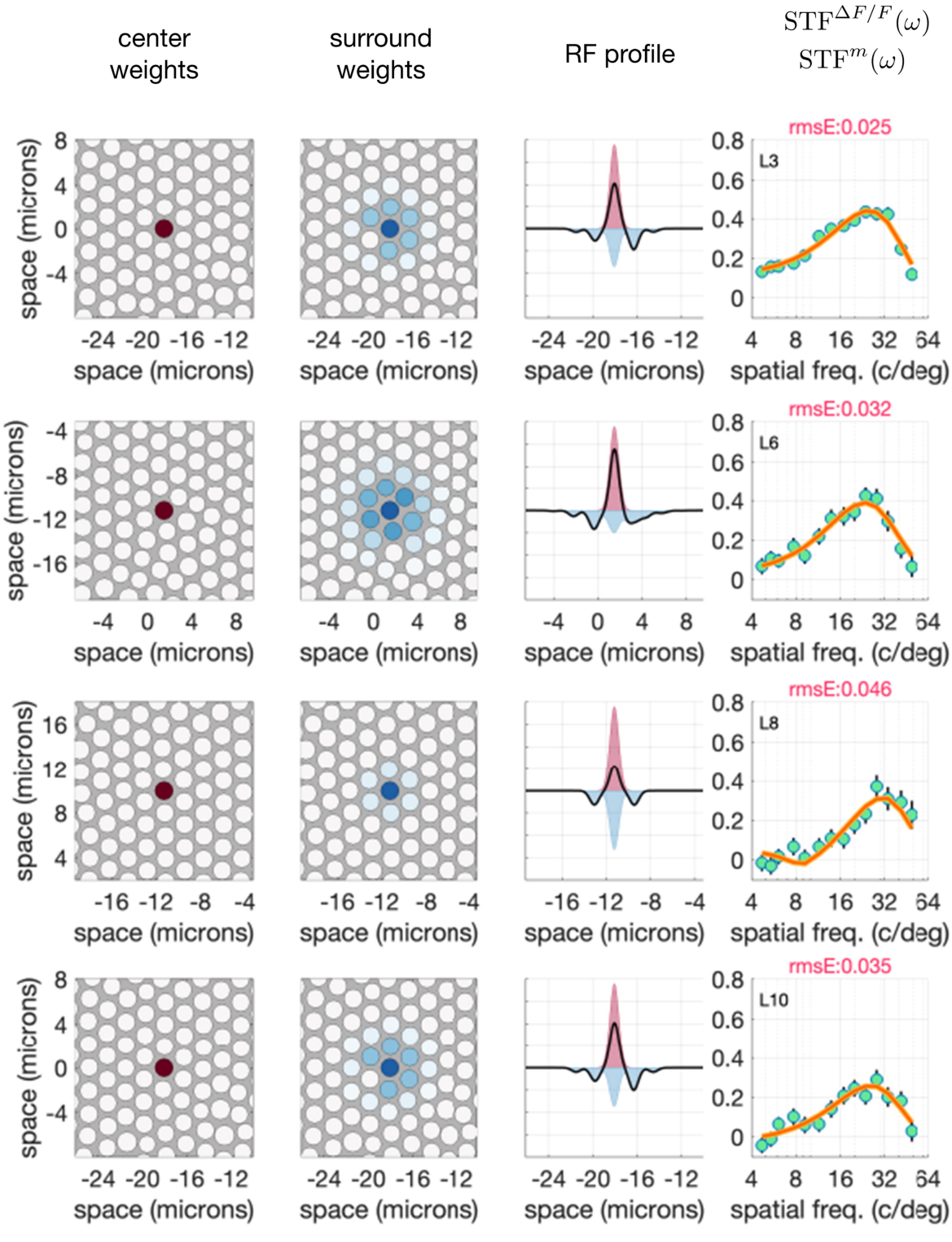
center weights
surround weights
RF profile
$\mathrm{STF}^{\Delta F/F}(\omega)$
$\mathrm{STF}^{m}(\omega)$
rmsE:0.025
L3
rmsE:0.032
L6
rmsE:0.046
L8
rmsE:0.035
L10
space (microns)
spatial freq. (c/deg)

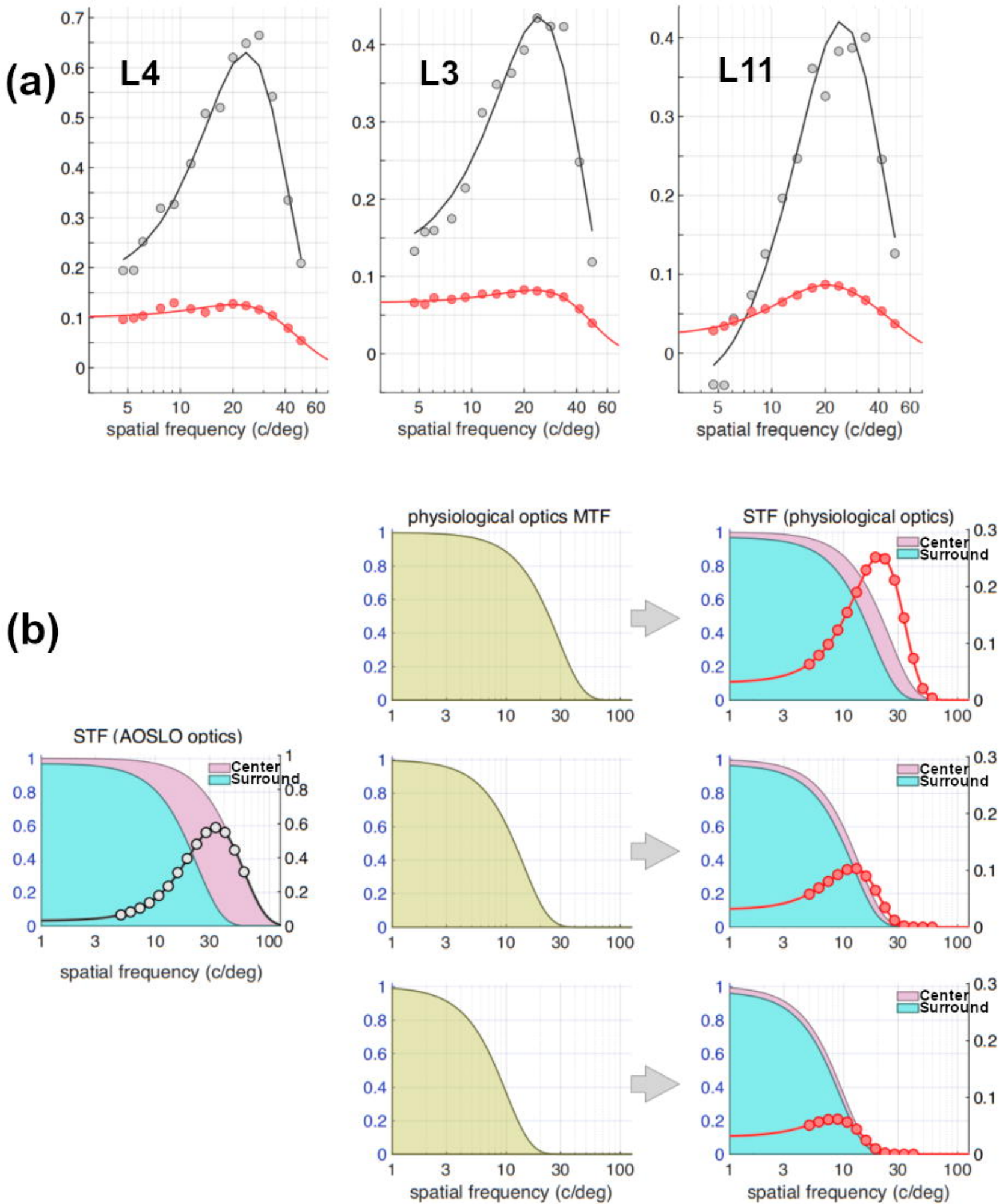
(a)
L4
L3
L11
spatial frequency (c/deg)
(b)
STF (AOSLO optics)
physiological optics MTF
STF (physiological optics)
Center
Surround
spatial frequency (c/deg)

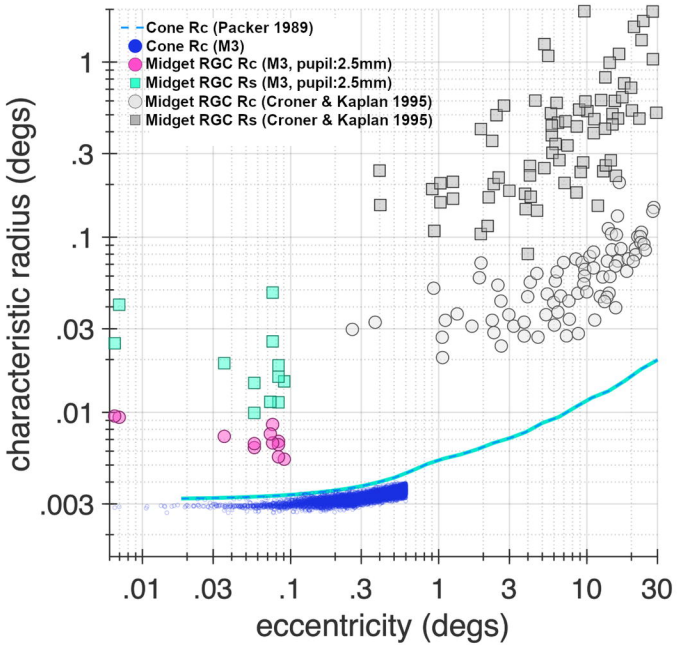
Cone Rc (Packer 1989)
Cone Rc (M3)
Midget RGC Rc (M3, pupil:2.5mm)
Midget RGC Rs (M3, pupil:2.5mm)
Midget RGC Rc (Croner & Kaplan 1995)
Midget RGC Rs (Croner & Kaplan 1995)
characteristic radius (degs)
1
.3
.1
.03
.01
.003
.01
.03
.1
.3
1
3
10
30
eccentricity (degs)

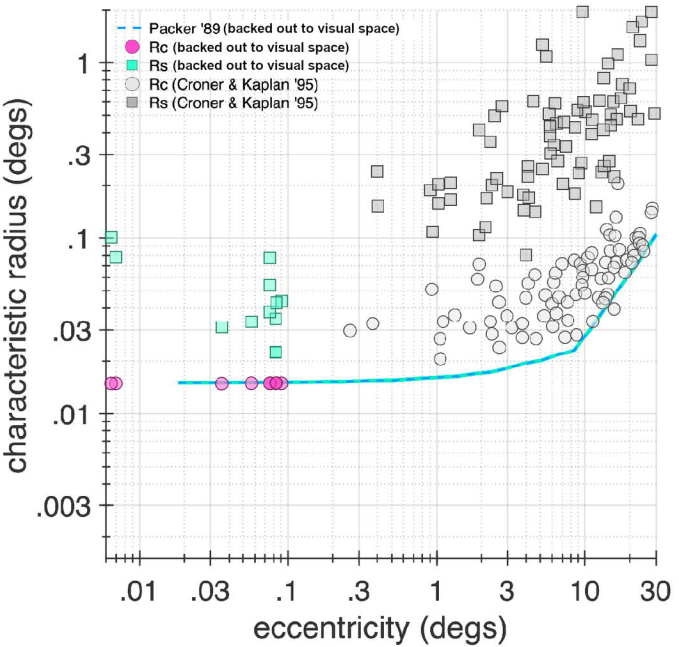
Packer '89 (backed out to visual space)
Rc (backed out to visual space)
Rs (backed out to visual space)
Rc (Croner & Kaplan '95)
Rs (Croner & Kaplan '95)
characteristic radius (degs)
1
.3
.1
.03
.01
.003
.01
.03
.1
.3
1
3
10
30
eccentricity (degs)

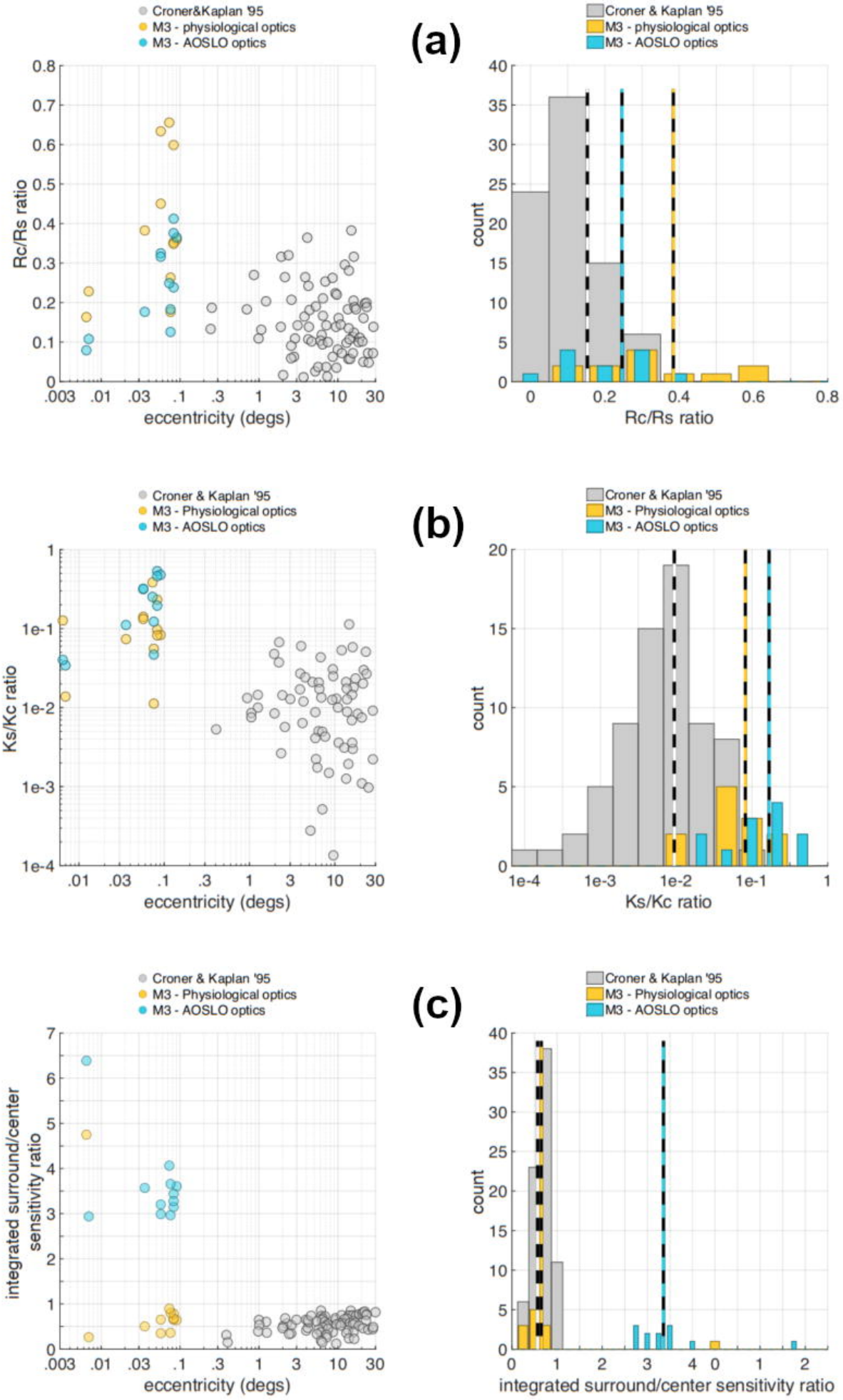
(a)
Croner&Kaplan '95
M3 - physiological optics
M3 - AOSLO optics
Rc/Rs ratio
eccentricity (degs)
Croner & Kaplan '95
M3 - physiological optics
M3 - AOSLO optics
count
Rc/Rs ratio
(b)
Croner & Kaplan '95
M3 - Physiological optics
M3 - AOSLO optics
Ks/Kc ratio
eccentricity (degs)
Croner & Kaplan '95
M3 - Physiological optics
M3 - AOSLO optics
count
Ks/Kc ratio
(c)
Croner & Kaplan '95
M3 - Physiological optics
M3 - AOSLO optics
integrated surround/center sensitivity ratio
eccentricity (degs)
Croner & Kaplan '95
M3 - Physiological optics
M3 - AOSLO optics
count
integrated surround/center sensitivity ratio